Article title

Quantitative imaging reveals distinct contributions of SnRK2 and ABI3 in plasmodesmatal permeability in *Physcomitrella patens*

Author names

Takumi Tomoi, Kensuke Kawade, Munenori Kitagawa, Yoichi Sakata, Hirokazu Tsukaya, and Tomomichi Fujita

Corresponding authors

Kensuke Kawade; kawa-ken@nibb.ac.jp; Phone: +81 (0)564 59 5883

Tomomichi Fujita; tfujita@sci.hokudai.ac.jp; Phone: +81 (0)11 706 2740

Six Figures

One Supplementary Table

Six Supplementary Figures

Short title

ABA signaling for plasmodesmatal permeability

Article title

Quantitative imaging reveals distinct contributions of SnRK2 and ABI3 in plasmodesmatal permeability in *Physcomitrella patens*

Author names and affiliations

Takumi Tomoi[a,b], Kensuke Kawade[b,c,d,1], Munenori Kitagawa[e], Yoichi Sakata[f], Hirokazu Tsukaya[b,g], and Tomomichi Fujita[h,1]

[a]Graduate School of Life Science, Hokkaido University, Kita10 Nishi8, Kita-ku, Sapporo, Hokkaido 060-0810, Japan

[b]Exploratory Research Center on Life and Living Systems (ExCELLS), 5-1 Higashiyama, Myodaiji, Okazaki, Aichi 444-8787, Japan

[c]National Institute for Basic Biology, 38 Nishigonaka, Myodaiji, Okazaki, Aichi 444-8585, Japan

[d]Department of Basic Biology, School of Life Science, Graduate University for Advanced Studies (SOKENDAI), 38 Nishigonaka, Myodaiji, Okazaki, Aichi 444-8585, Japan

[e]Cold Spring Harbor Laboratory, 1 Bungtown road, Cold Spring Harbor, New York 11724, USA

[f]Department of Bioscience, Tokyo University of Agriculture, 1-1-1 Sakuragaoka, Setagaya-ku, Tokyo 156-8502, Japan

[g]Department of Biological Sciences, Graduate School of Science, The University of Tokyo, 7-3-1 Hongo, Bunkyo-ku, Tokyo 113-0033, Japan

[h]Department of Biological Sciences, Faculty of Science, Hokkaido University, Kita10 Nishi8, Kita-ku, Sapporo, Hokkaido 060-0810, Japan

One-sentence summary

A protein kinase and a transcription factor are an essential and a promotive factor in the regulation of cell-to-cell connectivity in response to plant stress hormone abscisic acid.

Author contributions

T.T. and T.F. conceived the project. T.T. and K.K. designed the study. H.T. and T.F. directed the study. T.T. performed all experiments and analyzed the data. M.K. and Y.S. provided materials. T.T., K.K., and T.F. wrote the manuscript with input from co-authors.

Funding information

This work was supported by the BIO-NEXT project from the Exploratory Research Center on Life and Living Systems (ExCELLS) (K.K. and H.T.), a Grant-in-Aid for Scientific Research on Innovative Areas from the Japan Society for the Promotion of Science (25113002 to H.T.), Grant-in-Aid for Challenging Exploratory Research from Japan Society for the Promotion of Science (JSPS) (18H04829 to T. F.), and Grant-in-Aid for Scientific Research on Innovative Areas from JSPS (25650089 to T. F.).

Email address of Author for Contact

[1]Corresponding authors

Kensuke Kawade; kawa-ken@nibb.ac.jp; Phone: +81 (0)564 59 5883

Tomomichi Fujita; tfujita@sci.hokudai.ac.jp; Phone: +81 (0)11 706 2740

Abstract

Cell-to-cell communication is tightly regulated in response to environmental stimuli in plants. We previously used photoconvertible fluorescent protein Dendra2 as a model reporter to study this process. This experiment revealed that macromolecular trafficking between protonemal cells in *Physcomitrella patens* is suppressed in response to abscisic acid (ABA). However, it remains unknown what and how ABA signaling components contribute to this suppression.

Here, we showed that ABA signaling components SUCROSE NON-FERMENTING 1-RELATED PROTEIN KINASE 2 (PpSnRK2) and ABA INSENSITIVE 3 (PpABI3) play roles as an essential and a promotive factor, respectively in regulating ABA-induced suppression of Dendra2 diffusion between cells (ASD). Our quantitative imaging analysis revealed that disruption of *PpSnRK2* resulted in defective ASD onset itself, whereas disruption of *PpABI3* caused an 81-min delay in initiation of ASD. Live-cell imaging of callose deposition using aniline blue staining showed that, despite this onset delay, callose deposition on cross walls remained constant in the *PpABI3* disruptant, suggesting that PpABI3 facilitates ASD in a callose-independent manner. Given that ABA is an important phytohormone to cope with abiotic stresses, we further explored cellular physiological responses. We found that acquisition of salt stress tolerance is promoted by PpABI3 in a quantitative manner similar to ASD. Our results suggest that PpABI3-mediated ABA signaling may effectively coordinate cell-to-cell communication during acquisition of salt stress tolerance. This study will accelerate quantitative study for ABA signaling mechanism and function in response to various abiotic stresses.

KEYWORDS

abscisic acid signaling, cell-to-cell communication, *Physcomitrella patens*, quantitative imaging analysis, salt stress tolerance

Introduction

The phytohormone ABA plays a pivotal role in overcoming water-deficit stress conditions. Extensive molecular analyses have identified core components of ABA signaling in angiosperms which include an ABA receptor pyrabactin resistance 1-like (PYL) (also known as PYR or RCAR) (Ma et al., 2009; Park et al., 2009), a positive regulator of ABA signaling SnRK2 (Li et al., 2000; Mustilli et al., 2002; Yoshida et al., 2002), and its negative regulator of group A protein phosphatase type 2C (PP2C) (Umezawa et al., 2009; Vlad et al., 2009).

Under non-stressed conditions, PP2C interacts and suppress SnRK2 kinase activity (Yoshida et al., 2019). Once plants are exposed to water-deficit stress conditions, ABA binds to PYL receptor, which then inactivates PP2C to release SnRK2. This mechanism induces a SnRK2-mediated phosphorylation relay to activate the ABA signaling (Yoshida et al., 2019). Although details of molecular mechanisms are partially different, these ABA signaling components are highly conserved in basal land plants bryophytes such as moss *Physcomitrella patens* and liverwort *Marchantia polymorpha* (Khandelwal et al., 2010; Komatsu et al., 2013; Saruhashi et al., 2015; Stevenson et al., 2016; Eklund et al., 2018; Shinozawa et al., 2019).

Because plasmodesmata (PD) are cytoplasmic channels which transverse the cell walls to allow cell-to-cell communication, PD permeability is one of the critical elements to determine the extent of cell-to-cell communication. Interestingly, in addition to various phytohormones, downstream output of the ABA signaling is involved in the regulation of cell-to-cell communication by modulating callose deposition at PD in angiosperms (Han and Kim, 2016; Amsbury et al., 2018; Tylewicz et al., 2018; Wu et al., 2018). For example, in response to shorter photoperiods, PD permeability in shoot apices of *Populus* is reduced through the ABA signaling by formation of callosic sphincters to maintain bud dormancy (Tylewicz et al., 2018). The effect of ABA is compromised by expression of a dominant mutant allele *PP2C* of *Arabidopsis thaliana ABA INSENSITIVE 1* (*abi1-1*) (Tylewicz et al., 2018). This *abi1-1* phenotype was rescued by overexpression of *PD-LOCATED PROTEIN 1* (*PDLP1*), a type I membrane-receptor protein family (Tylewicz et al., 2018). Given that the PDLP-mediated callose deposition is likely to occur through direct interactions with *CALLOSE SYNTHASE* (*CALS*) *10/GLUCAN SYNTHASE LIKE* (*GSL*) *8* (Saatian et al., 2018), the PDLPs are important regulators for PD permeability through callose deposition in angiosperms. We recently reported that intercellular Dendra2 movement through PD in *P. patens* protonemal cells is suppressed by ABA treatment (Kitagawa et al., 2019). Transmission electron microscopy (TEM) revealed that ABA treatment decreased PD aperture size from 38 nm to 29 nm but had little effect on PD density (Kitagawa et al., 2019). Aniline blue staining indicated, however, that there is negligible change in callose deposition on cross walls after ABA treatment during decrease in PD permeability (Kitagawa et al., 2019). These

data suggest that the ABA-induced suppression of intercellular Dendra2 movement is likely to occur in a callose-independent fashion. Furthermore, genome database search identified no *PDLP* orthologous genes in *P. patens* (Lee, 2014; Brunkard and Zambryski, 2017). Therefore, it is of great interest to unravel how, in the absence of functional PDLPs the ABA signaling-mediated PD permeability is regulated in *P. patens*.

Photoconvertible fluorescent proteins such as Dendra2 and DRONPA have been used to analyze PD permeability. This quantitative approach revealed that, for example, in *A. thaliana* roots different cell types have different PD permeability, and their sensitivities in response to flagellin, low temperature and salicylic acid also differ (Wu et al., 2011; Gerlitz et al., 2018). In addition, we previously established an experimental setup to visualize and analyze intercellular Dendra2 movement in protonemal cells of *P. patens* (Kitagawa and Fujita, 2013; Kitagawa and Fujita, 2015), and found a phenomenon of ABA-induced suppression of Dendra2 movement between cells (ASD) (Kitagawa et al., 2019). However, due to a lack of quantitative characterization of the Dendra2 movement, its biophysical property such as diffusivity is still unclear. This prevents us from quantitatively dissecting the contributions of ABA signaling components on the regulation of PD permeability. In this study, we examined how the ABA signaling components *PpSnRK2* and *PpABI3* are involved in ASD by quantitatively characterizing the Dendra2 movement between protonemal cells through PD. Our analysis revealed different contributions of these two components on the regulation of PD permeability in response to ABA. Furthermore, we detected a delay in the ASD initiation in a *PpABI3* disruptant and that this delay is quite similar to the timescale required for salt stress tolerance acquisition in response to ABA. Based on these results, we discuss a possible function of *PpABI3* in coordinating the rapid initiation of ASD and salt stress tolerance acquisition in *P. patens*.

Results

Overexpression of *PpABI1A*^{G333D}, *PpSnRK2A*, and *PpABI3A* impacted on cellular growth and morphology

In response to the ABA treatment, protonemal cells of moss including *P. patens* exhibit drastic morphological changes and growth suppression and eventually differentiate into brood cells (or brachycytes) (Schnepf and Reinhard, 1997; Rowntree et al., 2007; Komatsu et al., 2009; Amagai et al., 2018). We observed a similar morphological changes in our transgenic line *ProEF1α:D2*, which constitutively expresses *Dendra2* (*D2*) under the control of an *EF1α* promoter. ABA treatment on the *ProEF1α:D2* inhibited cell growth but cell division was unaffected, and this resulted in the formation of round-shape cells like brood cells in their apices and slightly swollen cells in their basal regions (Fig. 1A). To examine whether these ABA-induced phenotypes requires the ABA signaling components, we constitutively overexpressed *PpABI1A*^{G333D} in the *ProEF1α:D2* background (*PpABI1A*^{G333D}*OX/ProEF1α:D2*). The *PpABI1A*^{G333D} allele harbors a hypermorphic mutation which phenocopies the *A. thaliana abi1-1* allele that acts as a negative regulator in ABA signaling (Koornneef et al., 1984; Eklund et al., 2018). We observed that cellular phenotypes in *PpABI1A*^{G333D}*OX/ProEF1α:D2* did not show significant difference between dimethyl sulfoxide (DMSO) control and ABA-treated samples (Fig. 1B). This indicates that the PpABI1A^{G333D} negatively impacted on the ABA signaling in *P. patens*, similar to that in *A. thaliana.*

We next examined whether the ABA-induced cellular phenotypes are reproducible by inducible overexpressions of *PpSnRK2A* and *PpABI3A* in the *ProEF1α:D2* background (*PpSnRK2AiOX/ProEF1α:D2* and *PpABI3AiOX/ProEF1α:D2*). Transcripts of *PpSnRK2A* and *PpABI3A* were readily detectable 24 hours after β-estradiol treatment (Supplemental Fig. S1, A-D). Expression levels of the transgenic *PpSnRK2A* and *PpABI3A* were much higher than the endogenous expression levels of *PpSnRK2A-D* and *PpABI3A-C* after ABA treatment (Supplemental Fig. S1, E-H). We confirmed that its cellular growth and morphology in the *ProEF1α:D2* were normal either in the absence or presence of β-estradiol (Fig. 1C). We observed that the growth of protonemal cells in the *PpSnRK2AiOX/ProEF1α:D2* ceased and exhibited swollen phenotypes upon β-estradiol treatment (Fig. 1D). On the other hand, the *PpABI3AiOX/ProEF1α:D2* primarily showed growth suppression with little morphological changes (Fig. 1E). We thus demonstrated that inducible expressions of either *PpSnRK2A* or

193 *PpABI3A* in the *PpSnRK2AiOX/ProEF1α:D2* and *PpABI3AiOX/ProEF1α:D2* lines can
194 partially phenocopies the ABA-induced morphological changes (Fig. 1, C-E).
195
196 **Overexpression of *PpABI1A*^{G333D}, *PpSnRK2A*, and *PpABI3A* influences intercellular**
197 **Dendra2 movement in protonemal cells**
198 Since overexpression of *PpABI1A*^{G333D}, *PpSnRK2A*, and *PpABI3A* impacted on the cellular
199 growth and morphology, we analyzed Dendra2 movement between protonemal cells in
200 *PpABI1A*^{G333D}*OX/ProEF1α:D2*, *PpSnRK2AiOX/ProEF1α:D2*, and
201 *PpABI3AiOX/ProEF1α:D2* to clarify contribution of these components on suppression of the
202 Dendra2 movement. In this system, intensity of the photoconverted Dendra2 red signal in
203 *ProEF1α:D2* decreased as the Dendra2 move away from the original cell over time in a
204 PD-mediated manner (Fig. 2A) (Kitagawa and Fujita, 2013; Kitagawa et al., 2019). Upon
205 ABA treatment, the Dendra2 intensity remained constant in the original cell, suggesting that
206 Dendra2 movement to neighboring cells was inhibited (Fig. 2A).
207 In the *PpABI1A*^{G333D}*OX/ProEF1α:D2*, although the Dendra2 movement was seemingly
208 suppressed upon ABA treatment as compared to the DMSO control, intercellular Dendra2
209 movement was still observed (Fig. 2B), suggesting a partial contribution of *PpABI1* on the
210 suppression of Dendra2 movement between cells. On the other hand, the Dendra2 movement
211 was fully suppressed in *PpSnRK2AiOX/ProEF1α:D2* and *PpABI3AiOX/ProEF1α:D2* upon
212 inducible overexpression of *PpSnRK2A* and *PpABI3A*, as compared to the corresponding
213 DMSO controls (Fig. 2, C-E). These observations indicate that inducible overexpression of
214 either *PpSnRK2A* or *PpABI3A* is sufficient to suppress the intercellular Dendra2 movement
215 even in the absence of ABA treatment.
216
217 **Quantification workflow to analyze Dendra2 movement between protonemal cells in**
218 **response to ABA**
219 We next established a method to quantitatively analyze the kinetics of Dendra2 intensity over
220 time based on a time-lapse Dendra2 imaging system reported previously (Kitagawa and Fujita,
221 2013). To rule out the possibility that disappearance of the Dendra2 intensity was due to

proteolytic protein turnover, we tracked the Dendra2 intensity in the presence of MG-132, a proteasome inhibitor. We found that the Dendra2 intensity in protoplasts was unchanged over the course of 720 min, both in MG-132-treated and DMSO control (Supplemental Fig. S2). This indicated that proteolytic degradation of Dendra2 is negligible for at least 720 min. In addition, we analyzed the Dendra2 intensity in the neighboring cells of the photoconverted cells. As the Dendra2 intensity was decreased in the original 12th cell, the increase in the Dendra2 intensity in the neighboring 11th and 13th cells was detected (Supplemental Fig. S3). Thus our data suggest that the decrease in the Dendra2 intensity in the original cell was due to the intercellular movement between the protonemal cells. In our previous report (Kitagawa and Fujita, 2013), directional movement of the Dendra2 towards apical side of protonemata was observed when protonemal cells were grown under the light condition but not under the dark condition. Consistently, in the time-lapse imaging under the dark condition in this study, directional bias of the Dendra2 movement was not found (Supplemental Fig. S3). It is also noted that the decrease in the Dendra2 intensity in the 11th and 13th neighboring cells was detectable over time, probably because the Dendra2 was diffused further.

We furthermore determined that this intercellular Dendra2 movement can be defined as a simple diffusion process because the kinetics of the Dendra2 intensity in the photoconverted cell was well fitted with a single exponential function (Fig. 3, A and B). This indicates that the intercellular Dendra2 mobility is characterized by two parameters, a time constant (τ) and an immobile fraction (B). The τ represents intercellular diffusivity of the Dendra2 through PD, and the B refers to the ratio of immobilized Dendra2 in the original cell (Fig. 3C).

In addition, we found that this quantification method can be employed to evaluate the effects of ABA on the intercellular Dendra2 diffusivity. Within 1 hour after ABA treatment, intensity of the photoconverted Dendra2 became restricted in the original cell (Fig. 3, A and B). Notably, Dendra2 in ABA-treated protoplasts was also stable to proteolytic degradation (Supplemental Fig. S2). Consistently, by fitting the Dendra2 kinetics with the single exponential function, the τ and B were smaller and larger in the ABA-treated sample, respectively as compared to the DMSO control (Fig. 3B). As the τ represents how fast the Dendra2 intensity reaches the B, the τ indicates how fast intercellular Dendra2 diffusivity is

suppressed in response to ABA and the *B* means the ratio of Dendra2 immobilized in the original cell as a result of ASD. Thus, our quantitative imaging analysis succeeded in characterizing the processes of intercellular diffusion of Dendra2 and its change in response to ABA.

Quantitative dissection revealed PpSnRK2 and PpABI3 contributions to ASD

Our phenotypic analyses indicated that *PpSnRK2A* and *PpABI3A* play more predominant roles than *PpABI1A* on ASD. We therefore next asked the question whether there is a differential contribution between *PpSnRK2A* and *PpABI3A* in regulating ASD. To this end, we measured the changes in the Dendra2 intensity over time in response to ABA in *ppsnrk2a/b/c/d* quadruple knockout (*ppsnrk2qko*) and *ppabi3a/b/c* triple knockout (*ppabi3tko*) mutants (*ProEF1α:D2*/*ppsnrk2qko* and *ProEF1α:D2*/*ppabi3tko*, respectively). We found that intercellular Dendra2 diffusion in the *ProEF1α:D2*/*ppsnrk2qko* was observable irrespective of the presence and absence of ABA treatment (Fig. 4, A and B). The τ and *B* obtained from the fittings were comparable between *ProEF1α:D2* (τ = 180, *B* = 0.16 in the median) and *ProEF1α:D2*/*ppsnrk2qko* (τ = 149, *B* = 0.23 in the median) in the absence of ABA or *ProEF1α:D2*/*ppsnrk2qko* in the presence of ABA (τ = 187, *B* = 0.22 in the median; $P = 7.9 \times 10^{-1}$ and $P = 4.2 \times 10^{-1}$), respectively (Fig. 4, E and F). This indicates that PpSnRK2 is an indispensable factor for ASD.

On the other hand, although intercellular Dendra2 diffusion was observed in *ProEF1α:D2*/*ppabi3tko* in the DMSO control (Fig. 4, C and D), the τ in *ProEF1α:D2*/*ppabi3tko* was calculated to be smaller than that in *ProEF1α:D2* (τ = 204 and 266 in the median), whereas the *B* was similar (*B* = 0.25 and 0.24 in the median) (Fig. 4, G and H). This suggests that the intercellular Dendra2 diffusivity is higher in *ProEF1α:D2*/*ppabi3tko* than in *ProEF1α:D2* under the normal culture condition, possibly due to responsiveness to endogenous ABA. Upon ABA treatment, the observed ASD in *ProEF1α:D2*/*ppabi3tko* was similar to that in *ProEF1α:D2* (Fig. 3A and Fig. 4C). However, the τ and *B* in *ProEF1α:D2/ppabi3tko* was significantly higher and lower (τ = 46, *B* = 0.72 in the median), respectively compared to that in the *ProEF1α:D2* control (τ = 10, *B* = 0.82 in the

median) (Fig. 4, G and H). Since the τ indicates responsiveness to ABA to initiate ASD, the higher τ in *ProEF1α:D2/ppabi3tko* suggests that the disruption of *PpABI3* causes a temporal delay to initiate ASD. The lower *B* in *ProEF1α:D2/ppabi3tko* can be also explained by this temporal delay before initiation of ASD. During the delay of ASD initiation, more Dendra2 can diffuse from the original cells to neighboring cells in *ProEF1α:D2/ppabi3tko* than *ProEF1α:D2*. Thus, the Dendra2 intensity in the original cell decreased to a greater extent in *ProEF1α:D2/ppabi3tko* than *ProEF1α:*D2 at the onset of ASD, which can result in the lower *B* in *ProEF1α:D2/ppabi3tko*.

Our results suggest that PpABI3 is responsible for the normal initiation of ASD. To gain better quantitative resolution on the temporal control of how PpABI3 facilitates this process, we introduced a time to the initiation of ASD (*A*) in this study (Fig. 4I). Because complete suppression of the Denra2 diffusion between cells requires infinite time due to the exponential indeterminate form (see Materials and Methods), we here considered the duration required for the Dendra2 intensity to the 90% of the steady state level (A_{90}). The A_{90} allows us to compare the temporal difference to initiate ASD in the absence and presence of *PpABI3*. We determined that in *ProEF1α:D2* the A_{90} is 24 min, whereas in *ProEF1α:D2*/*ppabi3tko* the A_{90} is increased to 105 min. This indicates an 81-min delay to arrest the Dendra2 diffusion in response to ABA in *ProEF1α:D2*/*ppabi3tko.* We obtained a similar temporal delay in the *ProEF1α:D2*/*ppabi3tko* when A_{85} and A_{95} were used, further confirming the robustness of our interpretation.

Suppression of intercellular Dendra2 diffusion by PpABI3 is callose-independent

Using TEM approach, we previously reported that the PD aperture size was reduced by 9-nm after ABA treatment. Aniline blue staining also showed that there are little changes in the callose deposition on cross walls (Kitagawa et al., 2019). However, it is still unclear whether conventional aniline blue staining in fixed cells is sufficient to support the callose-independent regulation of ASD. We therefore improved the aniline blue staining method and established its live-imaging method to observe changes in callose deposition on cross walls between targeted cells after ABA treatment. Callose accumulation at the cross wall

was detectable during cell divisions in living protonemal cells even in the presence of aniline blue solution (Supplemental Fig. S4A). Moreover, we were able to observe intercellular Dendra2 diffusion and ASD in this method (Supplemental Fig. S4B), indicating that link between intercellular Dendra2 diffusivity and the extent of callose deposition on cross walls is evaluable. We analyzed changes of callose deposition in the *ProEF1α:D2* on the same cross wall between the 11th and 12th cell for 180 min after ABA treatment, and found that callose signal intensity was constant throughout the observation, irrespective of ABA treatment. (Fig. 5, A and D). Intriguingly, callose intensity was also unchanged in the *ProEF1α:D2/ppabi3tko* as well as the *ProEF1α:D2/ppsnrk2qko* (Fig. 5, B-D). To investigate the callose deposition on cross walls between the 11th and 12th cell in greater details, we acquired images with better resolution from control and ABA-treated samples, at 20-, 100- and 180-min time points. When observed at 0.3-μm optical slice, we detected punctate signals on cross walls (Fig. 5, E-G; Supplemental Fig. S5, A and B), which resembles the PD-associated callose accumulation as detected previously by callose immunostaining (Kitagawa et al., 2019). There was no significant increase in the density of punctate signals between the control and ABA-treated samples in *ProEF1α:D2*, *ProEF1α:D2/ppsnrk2qko*, and *ProEF1α:D2/ppabi3tko* (Fig. 5H), and also *PpABI3AiOX/ProEF1α:D2* (Supplemental Fig. S5C). Our results suggest that PpABI3 does not increase the density of PD-associated callose in response to endogenous and exogenous ABA. Collectively, our data further supported that PpSnRK2 and PpABI3 facilitates ASD in a callose-independent manner.

PpABI3 is required in salt stress tolerance acquisition of protonemal cells in response to ABA

Given that PpABI3 facilitates the initiation of ASD in protonemal cells, we wonder whether this observation is related to any physiological response(s). One possible response is acquisition of salt stress tolerance since ABA plays crucial roles on this process (Takezawa et al., 2015). To test this hypothesis, we set out to determine the protonemal viability rate after salt stress treatment by counting propidium iodide (PI)-stained dead cells (Fig. 6A). In the control, all cells in *ProEF1α:D2*, *ppsnrk2qko/ProEF1α:D2*, and *ppabi3tko/ProEF1α:D2* were

alive (viability: 100 ± 0 %) (Fig. 6B). In *ProEF1α:D2*, the cell viability under salt stress without and after 5-, 20-, and 100-min ABA pretreatment was 51 ± 33%, 47 ± 41%, 83 ± 9%, and 87 ± 12%, respectively (Fig. 6B), indicating that salt stress tolerance was significantly induced after 20-min ABA pretreatment. In *ppsnrk2qko/ProEF1α:D2*, cell viability under salt stress without and after 5-, 20-, and 100-min ABA pretreatment was 13 ± 26%, 9 ± 19%, 5 ± 9%, and 14 ± 26% (Fig. 6B). This result showed that *ppsnrk2qko/ProEF1α:D2* is ABA-insensitive during acquisition of salt stress tolerance and is consistent with the essential role of PpSnRK2 in ASD (Fig. 4, A, B, E and F). On the contrary, cell viability in *ProEF1α:D2/ppabi3tko* under salt stress without and after 5-, 20-, and 100-min ABA pretreatment was 43 ± 26%, 35 ± 37%, 54 ± 27% and 76 ±18 % (Fig. 6B), indicating that salt stress tolerance was significantly induced after 100-min ABA treatment. There was about 80-min delay in acquisition of salt stress tolerance in *ProEF1α:D2/ppabi3tko* when compared to *ProEF1α:D2*. These results indicate that the PpABI3-mediated ABA signaling contributes to the acquisition of salt stress tolerance in around 80 min, which is quite similar to the value observed in PpABI3-mediated ASD response (Fig. 4I). This suggests a plausible mechanism connecting the regulation of PD permeability and viability against salt stress tolerance by PpABI3.

Discussion

This study provides quantitative dissection on the contributions of ABA signaling components in regulating protonemal PD permeability. Our analysis revealed that, in contrast to the essential roles of PpSnRK2 in ASD, PpABI3 plays a specific role in promoting the initiation of ASD within 80 min. We further unraveled that PpABI3 is required for the rapid acquisition of salt stress tolerance in protonemal cells, thereby contributing to the survival strategy during abiotic stress conditions. Interestingly, these two processes that mediated by PpABI3 occur in a similar timescale of tens of minutes, suggesting the promotive role of PpABI3 in coordinating PD permeability and stress tolerance through the ABA signaling.

Regulatory mechanism of ASD in protonemal cells of *P. patens*

Although our previous study reported the phenomenon of ASD and the contribution of endogenous ABA in ASD (Kitagawa et al., 2019), it remains elusive which of the ABA signaling components and how they are involved in this process. Here, we provide evidence to show that PpSnRK2 and PpABI3 are essential and promotive factors in the ABA signaling to drive ASD in protonemal cells. Our quantitative analysis based on the newly introduced A_{90} further revealed that ASD is almost initiated within this time frame after ABA treatment. Since PpSnRK2 is essential for ASD and is involved in the phosphorylation of ABA signaling, PpSnRK2 seems to phosphorylate ASD-related factors within 24 min based on A_{90} in *ProEF1α:D2*. Previously a phosphoproteomic analysis of the ABA signaling pathway identified 74 phosphopeptides (51 phosphorylated proteins except for PpSnRK2s) within 15 min after ABA treatment (Amagai et al., 2018). We speculate that the downstream targets of PpSnRK2 to trigger ASD are present in this phosphoprotein list. In consistent with this, seven of these phosphoproteins are orthologues found in the proteome of *A. thaliana* PD (Fernandez-Calvino et al., 2011; Amagai et al., 2018). However, their functions in regulating PD permeability and localizations around PD have not yet been demonstrated. It would be worth examining the contribution of their phosphomimic forms on ASD to uncover molecular mechanism of the ABA signaling in ASD.

In contrast to these downstream targets of the PpSnRK2, PpABI3 is not phosphorylated in the ABA signaling (Nakashima et al., 2009; Umezawa et al., 2013; Wang et al., 2013; Amagai et al., 2018). ABA INSENSITIVE 5 (ABI5) of *P. patens* is instead phosphorylated within 15 min after ABA treatment (Amagai et al., 2018). PpABI3A is known to interact with barley ABI5, which enhances transactivation of an ABA-responsive wheat Em promoter without ABA treatment (Marella et al., 2006). Therefore, one possible regulatory mechanism in ASD may be the co-regulation by a PpABI3 and PpABI5 heterodimer which accelerates the ASD downstream of PpSnRK2. If this is the case, the PpABI3-mediated ASD should involve transcriptional regulation since PpABI3 is a known transcriptional factor. Because basal expression of *PpABI3* is required for the protonemal growth in *P. patens* (Zhao et al., 2018), this weak but constitutive expression of *PpABI3* may also contribute to promote the rapid

initiation of ASD. This hypothesis is consistent with our observation that intercellular Dendra2 diffusion in the *ProEF1α:D2/ppabi3tko* is slightly higher than *ProEF1α:D2* under normal culture conditions. In addition, *de novo* synthesized PpABI3 in response to ABA may further augment the ABA signaling to boost ASD.

A key question relevant to the PpABI3-mediated regulation of ASD would be, what is the downstream mechanism? A previously reported proteome analysis study identified SYNAPTOTAGMIN (SYT) as a candidate target of PpABI3-mediated ABA signaling (Yotsui et al., 2016). SYT is annotated as a C2 domain containing protein. In *A. thaliana*, AtSYTA was shown to be a PD-localized protein (Schapire et al., 2008; Fernandez-Calvino et al., 2011; Levy et al., 2015; Perez-Sancho et al., 2015). It is tempting to hypothesize that PpSYT may tether plasma membrane and endoplasmic reticulum to restrict PD permeability as shown in other multiple C2 domains and transmembrane region proteins (Brault et al., 2019). Importantly, this regulation by the SYT may occur in a callose-independent manner, which is consistent with observation that the PpABI3-mediated ASD did not involve any callose deposition around PD.

Among the ABA signaling components, contribution of PpABI1 on ASD was less prominent compared to that of PpSnRK2 and PpABI3. In contrast to our finding, ABI1-mediated ABA signaling in *Populus* is involved in the regulation of PD permeability in bud dormancy (Tylewicz et al., 2018). This discrepancy can be explained by an interaction between ABI1 and SnRK2 and/or emergence of PDLP which can modify the ABA sensitivity in *Populus* (Komatsu et al., 2013; Lee, 2014; Brunkard and Zambryski, 2017). Our data warrant further investigations to unravel the molecular mechanisms of PpSnRK2-, PpABI3-, and PpABI1-mediated ABA signaling in ASD. This would be helpful to extend our understanding on how PD permeability is regulated in response to abiotic stresses.

Cellular physiological responses associated with ABA signaling in ASD

We previously established a simple simulation model for PD permeability based on a relationship between PD aperture and molecule size (Kawade and Tanimoto, 2015; Kawade et al., 2017). Although this model is well recapitulated in *in vivo* experiments using GFP

diffusivity through PD under the normal condition, it failed to explain the connection between ASD occurrence and the reduction in PD aperture size. Although upon ABA treatment the PD aperture was reduced from 38 nm to 29 nm (Kitagawa et al., 2019), the Dendra2 molecules with a Stokes radius of Dendra2 (2.4 nm) should still be able to diffuse through the tightened PD aperture without much difficulty (Sadovsky et al., 2017). However this is not the case as ABA treatment inhibits the intercellular ABA diffusion. These observations suggest that additional elements independent of PD structural modification such as cytoplasmic viscosity can be involved in ASD. Indeed, in response to ABA and some environmental stresses, sugar and sugar alcohol has been reported to accumulate in *P. patens* protonemal cells as compatible solutes (Nagao et al., 2005; Nagao et al., 2006; Oldenhof et al., 2006; Komatsu et al., 2013; Arif et al., 2018). This increment in the compatible solutes can enhance cytoplasmic viscosity (Wolkers et al., 1998; Golovina et al., 2001) which can affect macromolecular diffusivity (Verkman, 2002).

Lastly we pursued cellular physiological responses regulated by PpABI3 in protonemal tissues and found that salt stress tolerance is confered by the PpABI3 in a time frame similar to that of ASD. A series of studies had been carried out to investigate mechanisms involved to acquire various stress tolerance against desiccation, hyperosmolality, low temperature, and freezing in an order of 24 hours after ABA treatment (Minami et al., 2005; Komatsu et al., 2009; Khandelwal et al., 2010; Komatsu et al., 2013; Saruhashi et al., 2015; Tan et al., 2017). Involvement of PpABI3-mediated transcriptional regulation in these processes has also been reported (Khandelwal et al., 2010; Tan et al., 2017). However, our results showed that the acquisition of salt stress tolerance mediated by PpABI3 was much more rapid and occurred within 20 min of ABA pretreatment. Disruption of *PpABI3* compromised this rapid induction of salt stress tolerance and resulted in an aprroximately 80-min delay for the tolerance acquisition. Our studies, together with these results, indicate that PpABI3 plays roles in acquiring stress tolerance both in short and long time frame. We speculate that basal expression of the PpABI3 contributes to short term environmental stresses tolerance, and this "pre-existing" PpABI3 in combination with *de novo* synthesized PpABI3 are involved in the regulation of a transcriptional network to induce more robust and persisting stress tolerances.

Autoregulation of the ABI3 transcription may accelerate the downstream reaction until endogenous ABA is gradually synthesized (Minami et al., 2005; Bedi and Chaudhuri, 2018). Thus at the moment, it is tempting to speculate that whether and how PpABI3-mediated ASD and acquisition of salt stress tolerance are mechanistically and functionally coordinated in a relatively short duration. Nevertheless, it is also possible that the decreased viability in *ProEF1α:D2/ppsnrk2ako* or *ProEF1α:D2/ppabi3tko* is attributed to the repression of PpSnRK2- and/or PpABI3-mediated regulation of salt stress tolerance, which is independent of the regulation of cell-to-cell communication. Future experiments to address this point should provide further understanding of the relationship between cell-to-cell communication and physiological response at a cellular level.

Materials and Methods

Plant materials and growth conditions

The *Physcomitrella patens* WT strain used in this study was Gransden 2004 (Rensing et al., 2008). The *ProEF1α:D2*, *ppsnrk2qko*, and *ppabi3tko* lines were described previously (Khandelwal et al., 2010; Kitagawa and Fujita, 2013; Shinozawa et al., 2019). The plants were cultured on BCDAT medium with 0.8% (w/v) agar under continuous white light at 25°C for three to five days (Nishiyama et al., 2000).

Vector constructions

We obtained the full-length cDNA clone of *pphn8m2* including *PpABI1A* from the RIKEN BioResource Center (Resource number: pdp31463). A synonymous mutation in the open reading frame (ORF) of *PpABI1A* (*PpABI1A*^{G1610A}) in pdp31463 was corrected with the primer set of 5’-ATGAGGCGGTCTGCGATATTG-3’ (Forward) and 5’-CTATCTATCCCTGGGAACTTTTAAGTC-3’(Reverse). The resulting fragment was used to amplify the ORF of *PpABI1A* with the primer set of 5’-CACCATGGCCACAGCTAAAACTTGTAGAAG-3’ (Forward) and 5’-CTATCTATCCCTGGGAACTTTTAAGTC-3’ (Reverse). The ORF fragment of *PpABI1A*

was cloned into the pENTR/D-TOPO vector (Thermo Fisher Scientific) and confirmed by sequencing. To introduce a mutation mimicking *abi1-1* of *A. thaliana* (Koornneef et al., 1984) in the ORF fragment of *PpABI1A* (*PpABI1A*^{G333D}), PCR was performed with the primer set of 5'-ATGGGCATGATGGATCGC-3' (Forward) and 5'-CGTATACTCCAAAATAATGTAAAGGAGC-3' (Reverse) using the pENTR/D-TOPO vector containing *PpABI1A* as the template, and then the resultant fragment was ligated with DNA ligation kit (TaKaRa). The resultant plasmid was subjected to LR reaction with the destination pPOG1 vector using LR clonase II plus enzyme mix (Thermo Fisher Scientific) (pPOG1-PpABI1A^{G333D}).

The ORF fragment of *PpSnRK2A* from pGAD424 vector containing *PpSnRK2A* was amplified with the primer set of 5'-CACCATGGATATTCCGAGCATGCATGACCAC-3' (Forward) and 5'-CATTGCGCACACAAACTCCCCAC-3' (Reverse). The ORF fragment of *PpSnRK2A* was cloned into the pENTR/D-TOPO vector (Thermo Fisher Scientific) and confirmed by sequencing. The resultant plasmid was subjected to LR reaction with the destination pPGX8 (Kubo et al., 2013) vector using LR clonase II plus enzyme mix (Thermo Fisher Scientific) (pPGX8-PpSnRK2A).

We obtained the full-length cDNA clones of *pphn37a15* including *PpABI3A* from the RIKEN BioResource Center (Resource number: pdp41729). The ORF fragment of *PpABI3A* in pdp41729 was amplified with the primer set of 5'-CACCATGGTGCTCCTATCGAGTGTG-3' (Forward) and 5'-TCCTGCGGGCTCGGTC-3' (Reverse). The ORF fragment of *PpABI3A* was cloned into the pENTR/D-TOPO vector (Thermo Fisher Scientific) and confirmed by sequencing. The resultant plasmid was subjected to LR reaction with the destination pPGX8 (Kubo et al., 2013) vector using LR clonase II plus enzyme mix (Thermo Fisher Scientific) (pPGX8-PpABI3A).

The pPOG1-PpABI1A^{G333D}, pPGX8-PpSnRK2A, and pPGX8-PpABI3A were digested with the restriction enzyme *Sse*8387I (TaKaRa) before transformation.

Transgenic lines

Transformation was performed based on the polyethylene glycol-mediated method (Nishiyama et al., 2000).

The *PpABI1A*^{G333D}*OX/ProEF1a:D2* lines were generated by introducing the *Sse*8387I-digested pPOG1-PpABI1A^{G333D} fragments into the *ProEF1α:D2* genetic background. Stable transformants were selected on BCDAT agar medium containing 30 mg/L hygromycin B (Wako) twice. The expression of *PpABI1A*^{G333D} in *PpABI1A*^{G333D}*OX/ProEF1α:D2* lines was confirmed through RT-PCR with the primer set of 5’-TGTGGTGCCTAGTGACGCTG-3’ (Forward) and 5’-ATTCGCTGCCTGCGATCCAT-3’ (Reverse) for *PpABI1A*^{G333D} and the primer set of 5’-TGCCATTAAGACGGCTATCA-3’ (Forward) and 5’-CGAGATTATTTCCAACAGATGGTCTA-3’ (Reverse) for *PpGAPDH* (as an internal control) (Supplemental Fig. S6).

PpSnRK2AiOX/ProEF1α:D2 lines were generated by introducing the *Sse*8387I-digested pPGX8-PpSnRK2A fragments into the *ProEF1α:D2* genetic background. Stable transformants were selected on BCDAT agar medium containing 30 mg/L hygromycin B (Wako) twice. The gene targeting was verified by genomic PCR with the primer set of 5’-ACAAGTTTGTACAAAAAAGCAGGCT-3’ (Forward) and 5’-CATTGCGCACACAAACTCCC-3’ (Reverse) which bind the outside from the 5’-end of ORF and the 3’-end of ORF of *PpSnRK2A*, and the primer set of 5’-CGCTTAGGCAGGAGGCCGTT-3’ (Forward) and 5’-CACCCTCTGGCCCGTGACAA-3’ (Reverse) which bind the inside of transgene and the outside of the 3’-end of the *P. patens* inter-genic 1 (PIG1) site.

PpABI3AiOX/ProEF1α:D2 lines were generated by introducing *Sse*8387I-digested pPGX8-PpABI3A fragments into the *ProEF1α:D2* genetic background. Stable transformants were selected on BCDAT agar medium containing 30 mg/L hygromycin B (Wako) twice. The gene targeting was verified by genomic PCR with the primer set 5’-ACAAGTTTGTACAAAAAAGCAGGCT-3’ (Forward) and 5’-TCCTGCGGGCTCGGTCTTCA-3’ (Reverse) which bind the outside from the 5’-end of ORF and the 3’-end of ORF of *PpABI3A*, and with the primer set 5’-CGCTTAGGCAGGAGGCCGTT-3’ (Forward) and

5’-CACCCTCTGGCCCGTGACAA-3’ (Reverse) which bind the PIG1 site.

The *ProEF1α:D2/ppsnrk2qko* and *ProEF1α:D2/ppabi3tko* lines were established by introducing the *ProEF1α:D2* construct (pT1OG-Dendra2) (Kitagawa and Fujita, 2013) into the *ppsnrk2qko* and *ppabi3tko* genetic backgrounds, respectively (Khandelwal et al., 2010; Shinozawa et al., 2019). Stable transformants were selected on BCDAT agar medium containing 100 mg/L zeocin (Invitrogen) twice.

The independently generated transgenic lines underwent the following quantitative RT-PCR, microscopy and photoconversion assay, callose staining with aniline blue, and viability test against salt stress, in which we confirmed reproducibility.

Quantitative RT-PCR

Protonemal tissues of *ProEF1α:D2, PpSnRK2AiOX/ProEF1α:D2*, and *PpABI3AiOX/ProEF1α:D2* lines were cultured for 10 days under red light on BCDAT agar medium overlaid with cellophane sheets. The cellophane with the 10-day-old culture of *ProEF1α:D2* were then transferred onto BCDAT agar medium with 50 μM ABA, and subjected to additional culture for 1, 6, or 12 hours to investigate the expression levels of *PpSnRK2A-D* (Pp3c5_21160V3, Pp3c6_16600V3, Pp3c6_11090V3 and Pp3c5_17150V3, respectively) and *PpABI3A-C* (Pp3c2_3370V3, Pp3c17_16470V3 and Pp3c4_7320V3, respectively) in response to ABA. In the negative control, the cellophanes with the 10-day-old culture of *ProEF1α:D2* were directly used to investigate the expression level of *PpSnRK2A-D* and *PpABI3A-C* without additional culture on BCDAT agar medium with 50 μM ABA. For inducible experiments, the cellophanes with the 10-day-old cultures of *ProEF1α:D2, PpSnRK2AiOX/ProEF1α:D2*, and *PpABI3AiOX/ProEF1α:D2* lines on BCDAT agar medium were transferred onto BCDAT agar medium with 1 μM β-estradiol (or 0.1% (v/v) DMSO as the negative control). The plant tissues were used for RT-PCR analysis 24 hours after transfer to confirm the inducible overexpression of *PpSnRK2A* or *PpABI3A*.

Total RNA was purified from the protonemal tissues with RNeasy Plant Mini Kit (QIAGEN). First-strand cDNA was synthesized with ReverTra Ace qPCR RT Master Mix with gDNA Remover (TOYOBO) according to the manufacture’s instruction. qRT-PCR was

performed using an ABI 7500 RealTimePCR System (Applied Biosystems) with the THUNDERBIRD qPCR mix (TOYOBO). The data were analyzed by the ΔΔCt method for relative quantification of the transcript levels. The transcript levels were normalized against riboflavin kinase gene (*RFK*) (Pp3c12_7730V3) or 3-hydroxyisobutyryl-CoA hydrolase gene (*HIBCH*) (Pp3c4_17830V3), whose expression levels were reported to be robust against ABA treatment (Khraiwesh et al., 2015). The data were collected from three independent biological replicates with technical triplicates, and subjected to the statistical analysis of Welch's *t*-test. The used primers in the qRT-PCR is listed in Supplemental Table S1.

Microscopy and photoconversion assay

Three- to five-day-old protonemal tissues were inoculated into 500 μL of BCDAT medium containing 0.5% glucose (BCDATG) solidified with 0.5% gellan gum in 4-well chamber slides (no. 5222-004; Iwaki), and then covered with the additional 250 μL of the medium. To suppress branching of the protonemata, the samples were cultured under continuous red light for 10 days as previously reported (Kitagawa and Fujita, 2013) except for *ProEF1α:D2/ppsnrk2qko* (for 15 days) due to its slower growth under red light. *ProEF1α:D2* was also cultured for 15 days when compared with *ProEF1α:D2/ppsnrk2qko*. In the test of ABA effects, 50 mM ABA or DMSO was added into wells of the 4-well chamber slides just after photoconversion to final concentrations of 50 μM and 0.1% (v/v), respectively. In the test of overexpression effect of *PpSnRK2A* or *PpABI3A*, 1 mM β-estradiol or DMSO was added into wells of the 4-well chamber slides 24 hours before photoconversion to final concentrations of 1 μM and 0.1% (v/v), respectively. For assessment of protonemal growth and morphology, the samples were observed under a microscope (DM 2500, Leica).

Photoconversion of Dendra2 was carried out using a confocal laser-scanning microscope (Nikon A1, Nikon) in the 12th cells from the apices in protonemata with 405-nm diode laser (10.0% laser output, 36 mW) with 3 iterations (8 sec/frame, zoom 4×) using the PlanApo 10x/0.45 NA objective. Time-lapse imaging was subsequently performed with the objective lens PlanApo 10x /0.45 NA and 561-nm solid laser (2.0% laser output, 10 mW) at 20-min intervals for 720 min. Five z-stack images of size 1024 × 1024 pixels were acquired at 6-μm

steps in each interval. The pinhole size was set to 16.60 μm in diameter, which yields a 7.29 μm optical slice in this condition.

We manually measured the mean fluorescence intensity of photoconverted Dendra2 in the whole regions of the laser-irradiated cells or the neighboring cells, and subtracted the mean fluorescence intensity of the surrounding medium region at each time point with Fiji software (ImageJ; https://imagej.net/Fiji). Based on the previous analysis (Kawade et al., 2017), the kinetics of Dendra2 intensity from 0 to 720 min after photoconversion was fitted by an exponential function as

$$I(t) = (I_0 - B)e^{(-t/\tau)} + B, \quad (1)$$

where $I(t)$ and I_0 are fluorescence intensity of Dendra2 at a time t and just after photoconversion, respectively, normalized with the mean fluorescence intensity per pixel just after photoconversion ($I_0 = 1$); τ is a time constant of Dendra2 diffusivity or responsiveness to ABA treatment for ASD; B is an immobile fraction of Dendra2 in the original cell. τ and B are free parameters determined by minimizing the residual sum of squares (RSS) between the measured data and the fitting function (1) by using custom MATLAB scripts.

Dendra2 intensity decreased over time and reached the level at the steady state in our experiment. To evaluate how this profile is affected in response to ABA during the progression to ASD, we here calculated a decrease ratio of Dendra2 intensity (x%) at an arbitrary point of time t against the Dendra2 intensity at the steady state. The decrease ratio of Dendra2 intensity at a time t is described as follows:

$$(I(t) - B)/(I_0 - B) = 1 - x/100. \quad (2)$$

When solving for $I(t)$, we obtained the following equation:

$$I(t) = (1 - x/100) \times (I_0 - B) + B. \quad (3)$$

By solving for x after introduction of (3) into (1), the decreased ratio of Dendra2 intensity x was summarized by using t and τ, given as:

$$x = 100 \times (1 - e^{(-t/\tau)}). \quad (4)$$

Because, in this case, t represents time required for reaching the Dendra2 intensity to the x% of the steady state level, we introduced a new parameter Ax for this specific time instead of t to avoid confusion as follows:

$$x = 100 \times (1 - e^{(-Ax/\tau)}). \quad (5)$$

By using this equation, we were able to evaluate how rapidly ASD is observed in response to ABA. A_{90} nearly equals to 2.3-fold value of τ.

Assessment of Dendra2 degradation in protoplasts

Protoplasts were obtained from three- to five-day-old protonemal tissues of *ProEF1α:D2* through 20-min treatment of 2% (w/v) Driserase dissolved in 8% (w/v) mannitol (Kyowa Hakko Kogyo Co., Ltd.) solution with gentle mix at 5-min intervals. The protoplasts were filtered through a mesh (CellTrics ®, 50 μm, Partec) into a 12 mL tube, collected by centrifugation at 1,000 rpm, and suspended in 8% (w/v) mannitol solution. After centrifugation again, the protoplasts were suspended in 250 μL of BCDATG medium containing 0.5% (w/v) gellan gum and 6% (w/v) mannitol, and put into each well of 8-well chamber slides (no. 5232-008; Iwaki), and then covered with additional 500 μL of BCDATG medium containing 0.5% (w/v) gellan gum and 6% (w/v) mannitol .

Images of protoplasts were obtained just after and 12 hours after photoconversion. Mean fluorescence intensity per pixel of photoconverted Dendra2 in the protoplasts was analyzed with Fiji software (ImageJ; https://imagej.net/Fiji). Dendra2 degradation was assessed with the ratio of mean fluorescence intensity just after photoconversion and at 12 hours after photoconversion. MG-132 (final concentration 50 μM) was added into the wells of 8-well chamber slides 1.5 hours before photoconversion of Dendra2 for the negative control of proteolytic degradation.

Callose staining with aniline blue

Aniline blue (Wako) was dissolved in 100 mM phosphate buffer (pH 8.7) to a concentration of 5.0% (w/v), and sterilized by filtration (pore size = 0.22 μm). The 5.0% (w/v) aniline blue solution was further dissolved in the buffer to a concentration of 1.6% (w/v). The color of aniline blue solution was changed from blue to brownish yellow when incubated more than 2 days at room temperature and exposure to air at several times. Staining was carried out after the color change. We found that the color aniline blue solution changed into yellow-brown

when dissolving in the pH 8.7 phosphate buffer. This is similar to the case of dissolving aniline blue in K_3PO_4 (pH 12) solution as the previous reported (Zavaliev and Epel, 2015).

The aniline blue solution was added to samples to a concentration of 0.1% (w/v) one day before observation under Nikon A1 confocal microscope (Nikon). To detect change in callose signal with aniline blue, time-lapse imaging was performed with the PlanApo-VC 20x/0.75 NA objective (zoom 4×) and 405-nm diode laser (2.0% laser output, 36 mW) at 20-min intervals for 180 min. Five z-stack images of size 1024 × 1024 pixels were acquired at 3 μm-steps in each interval. The pinhole size was set to 14.05 μm in diameter, which yields a 1.77 μm optical slice in this condition. To calculate the density of punctate signals from callose, images were acquired with the PlanApo-VC 100xH/1.4 NA objective (zoom 4×) and 405-nm diode laser (100% laser output, 36 mW). The pinhole size was set to 40.87 μm in diameter, which yields a 0.31 μm optical slice in this condition. We calculate the density of punctate signals from the obtained images with manual adjustments of brightness and contrast. For counting the punctate signals, we manually adjust contrast and/or brightness so that we can distinguish each punctate signal in the same image possessing different signal intensity of the cross wall.

Viability test against salt stress

Three- to five-day-old protonemal tissues were inoculated into 200 μL of BCDATG with 0.5% gellan gum, in glass-based dishes with 27-mm-diameter chambers (no. 3960-035; Iwaki) and then covered with additional 300 μl of the medium. In addition, 8.5 mL of liquid BCDATG medium was poured on the culture medium to avoid drying. The samples were cultured for 10 days under continuous light with the glass side up.

The liquid medium was exchanged with 8.5 mL of liquid BCDATG medium containing ABA to final concentration 50 μM. The samples were incubated for 20 and 100 min. These steps were skipped in the case without ABA treatment. To give salt stress to protonemal tissues, the liquid medium was exchanged with 8.5 mL of liquid BCDATG medium containing NaCl to a final concentration of 600 mM for 60 min. To assess cell viability, the liquid medium containing NaCl in the samples were exchanged with 3 mL of 50 μg/mL

propidium iodide (PI) and incubated for 5 min, and then washed out with 8.5 mL of liquid BCDATG medium for 5 min. In the control, the samples were directly subjected to the PI staining without salt stress treatment.

Under a stereomicroscope (M165 FC, Leica), we counted the number of dead cells among 14 cells from the apices in each protonema as judged with the PI signal in nuclei.

Supplementary data

Supplemental Figure S1. Expression level of *PpSnRK2* and *PpABI3* in protonemal tissues.

Supplemental Figure S2. Measurement of the Dendra2 degradation rate.

Supplemental Figure S3. Change in fluorescence intensity of Dendra2 in the neighboring cells of the photoconverted cells.

Supplemental Figure S4. Callose signal on newly formed cross walls and intercellular Dendra2 diffusivity under the condition of callose staining with aniline blue.

Supplemental Figure S5. Live-cell imaging of callose staining in *PpABI3AiOX/ProEF1α:D2.*

Supplemental Figure S6. Expression of *PpABI1A*^{G333D} in protonemal tissue of *PpABI1A*^{G333D}*OX/ProEF1α:D2*.

Supplemental Table S1. Primer sequences in qPCR.

Acknowledgements

We are grateful to O.K. Teh. (Hokkaido University) for correcting this manuscript. We thank Y. Hiwatashi (Miyagi University) and M. Hasebe (National Institute for Basic Biology) for the pPGX8 and pPOG1 vectors. RIKEN BioResource Center for the pdp31463 and pdp41729 plasmids; the Spectrography and Bioimaging Facility and the Functional Genomics Facility (NIBB Core Research Facilities), and the Model Plant Research Facility (NIBB BioResource Center) for technical supports.

Figure legends

Figure 1. Morphology and growth of protonemal cells in transgenic lines overexpressing *PpABI1A^{G333D}*, *PpSnRK2A*, or *PpABI3A*.

A and B, Representative images of protonemal cells at apical and basal positions after DMSO or ABA treatment in *ProEF1α:D2* (A) and *PpABI1A^{G333D}OX/ProEF1α:D2* (B). C to E, Representative images of protonemal cells at apical and basal positions after DMSO or β-estradiol treatment in *ProEF1α:D2* (C), *PpSnRK2AiOX/ProEF1α:D2* (D), and *PpABI3AiOX/ProEF1α:D2* (E). Times after treatment are indicated. The 12th cells were observed as the basal cells. Scale bars = 50 μm. Arrowheads indicate cross walls of the original branches.

Figure 2. Dendra2 movement between protonemal cells in transgenic lines overexpressing *PpABI1A^{G333D}*, *PpSnRK2A*, or *PpABI3A*.

A and B, Representative differential interference contrast (DIC) and photoconverted Dendra2 fluorescence (gray) images in protonemal cells of *ProEF1α:D2* (A) and *PpABI1A^{G333D}OX/ProEF1α:D2* (B) treated with DMSO or ABA. C to E, Representative DIC and photoconverted Dendra2 fluorescence (gray) images in protonemal cells of *ProEF1α:D2* (C), *PpSnRK2AiOX/ProEF1α:D2* (D), and *PpABI3AiOX/ProEF1α:D2* (E) treated with DMSO or β-estradiol. Times after photoconversion are indicated. Scale bars = 100 μm.

Figure 3. Quantitative characterization of Dendra2 movement between protonemal cells and its suppression by ABA.

A, Representative DIC, non-photoconverted (green), and photoconverted (gray) Dendra2 fluorescence images in protonemal cells of *ProEF1α:D2* treated with DMSO or ABA. Times after photoconversion are indicated. Scale bars = 100 μm. B, Mean fluorescence intensity of Dendra2 at 20-min intervals after photoconversion in photoconverted protonemal cells of *ProEF1α:D2* treated with DMSO (n = 15) or ABA (n = 27). Standard deviation (SD) is indicated by shaded area. The time constant (τ) and immobile fraction (B) were determined by

fitting the exponential function to the kinetics of mean fluorescence intensity (black solid lines). RSS, residual sum of squares. C, Schematic diagram of kinetics obtained by using different combinations of fitting parameters. Intercellular diffusivity of macromolecules is determined by τ and B. Highly permeable PD allow Dendra2 to move more rapidly from the original cell (black) than lower permeable PD (blue). More Dendra2 is trapped in the original cell when immobile fraction is increased (red).

Figure 4. Intercellular Dendra2 diffusivity in protonemal cells of *ProEF1α:D2/ppsnrk2qko* and *ProEF1α:D2/ppabi3tko.*

A and C, Representative DIC and photoconverted Dendra2 fluorescence (gray) images in protonemal cells of *ProEF1α:D2/ppsnrk2qko* (A) and *ProEF1α:D2/ppabi3tko* (C) treated with DMSO or ABA. Times after photoconversion are indicated. Scale bars = 100 μm. B and D, Mean fluorescence intensity of Dendra2 at 20-min intervals after photoconversion in protonemal cells of *ProEF1α:D2/ppsnrk2qko* (B) and *ProEF1α:D2/ppabi3tko* (D) treated with DMSO or ABA with exponential fits to the mean data. SD is indicated by the shaded area. The τ and B were determined by fitting the exponential function to the kinetics of mean fluorescence intensity (black solid lines). E to H, Values of the time constant τ and B obtained through the fittings. The τ and B in *ProEF1α:D2* and *ProEF1α:D2/ppsnrk2qko* (E and F), and in *ProEF1α:D2* and *ProEF1α:D2/ppabi3tko* (G and H). Each violin plot shows the density distribution of the data by the box plot (median as a yellow horizontal line, interquartile range as a box, and data range as whiskers). The P value was determined by the Mann-Whitney U-test. *ProEF1α:D2* with DMSO (n = 17) and ABA (n = 24) (E and F), and *ProEF1α:D2/ppsnrk2qko* with DMSO (n = 13) and ABA (n = 22) (B, E and F). *ProEF1α:D2* with DMSO (n = 15) and ABA (n = 27) (G and H), and *ProEF1α:D2/ppabi3tko* with DMSO (n = 14) and ABA (n = 17) (D, G and H). I, Time to initiation of ASD calculated from the median of fitting parameters in *ProEF1α:D2* and *ProEF1α:D2/ppabi3tko*. The grey line indicates A_{90}.

Figure 5. Live-cell imaging of aniline blue staining for callose after ABA treatment.

A to C, Representative images of DIC and aniline blue fluorescence for callose staining in protonemal cells of *ProEF1α:D2* (A), *ProEF1α:D2/ppsnrk2qko* (B), and *ProEF1α:D2/ppabi3tko* (C) after DMSO or ABA treatment. Times after treatment are indicated. The callose signal is shown in Fire look-up table of ImageJ. Scale bars = 20 μm. D, Change in aniline blue fluorescence intensity on cross walls in protonemal cells of *ProEF1α:D2*, *ProEF1α:D2/ppsnrk2qko*, and *ProEF1α:D2/ppabi3tko* after DMSO or ABA treatment. *ProEF1α:D2* with DMSO (n = 12) and ABA (n = 12), *ProEF1α:D2/ppsnrk2qko* with DMSO (n = 12) and ABA (n = 8), and *ProEF1α:D2/ppabi3tko* with DMSO (n = 10) and ABA (n = 12). The P value was determined by the Welch's t-test, n.s., non-significance ($P \geq 0.05$). E to G, Representative images of DIC and punctate callose signal of aniline blue fluorescence at cross walls between the 11th and 12th cell of *ProEF1α:D2* (E), *ProEF1α:D2/ppsnrk2qko* (F), and *ProEF1α:D2/ppabi3tko* (G) protonemal cells after ABA treatment. Times after treatment are indicated. Scale bars = 5 μm. Arrowheads indicate punctate signals included in the number as an example (E). H, The density of punctate signals on cross walls between the 11th and 12th cell in *ProEF1α:D2*, *ProEF1α:D2/ppsnrk2qko*, and *ProEF1α:D2/ppabi3tko* after ABA treatment. Each violin plot shows the density distribution of the data by the box plot (median as a cyan horizontal line, interquartile range as a box, and data range as whiskers). *ProEF1α:D2* without and after 20-, 100- and 180-min ABA treatment (n = 19, 17, 18 and 30, respectively), *ProEF1α:D2/ppsnrk2qko* without and after 20-, 100- and 180-min ABA treatment (n = 18, 8, 9 and 9, respectively), and *ProEF1α:D2/ppabi3tko* without and after 20-, 100- and 180-min ABA treatment (n = 10, 18, 19 and 18, respectively). The P value was determined by the Mann-Whitney U-test, n.s., non-significance $P \geq 0.05$).

Figure 6. Viability under salt stress after different pretreatment time of ABA.

A, Representative bright field, PI and non-photoconverted Dendra2 fluorescence images after the salt stress treatment. Cells with PI signal indicate dead cells. B, Survival rate after the salt stress with ABA pretreatment. "w/o NaCl" indicates the condition without salt stress and ABA treatment. The bar graph shows mean ± SD of the survival rate (n = 75). The P value was determined by the Mann-Whitney U-test, n.s., non-significance ($P \geq 0.05$), *$P < 0.01$

compared to the non-ABA pretreated corresponding line.

References

Amagai A, Honda Y, Ishikawa S, Hara Y, Kuwamura M, Shinozawa A., et al. (2018) Phosphoproteomic profiling reveals ABA-responsive phosphosignaling pathways in *Physcomitrella patens*. Plant J **94:** 699-708

Amsbury S, Kirk P, Benitez-Alfonso Y (2018) Emerging models on the regulation of intercellular transport by plasmodesmata-associated callose. J Exp Bot **69:** 105-115

Arif MA, Alseekh S, Harb J, Fernie A, Frank W (2018) Abscisic acid, cold and salt stimulate conserved metabolic regulation in the moss *Physcomitrella patens*. Plant Biol **20:** 1014-1022

Bedi S, Chaudhuri RN (2018) Transcription factor ABI3 auto-activates its own expression during dehydration stress response. FEBS Lett **592:** 2594-2611

Brault ML, Petit JD, Immel F, Nicolas WJ, Glavier M, Brocard L., et al. (2019) Multiple C2 domains and transmembrane region proteins (MCTPs) tether membranes at plasmodesmata. EMBO Rep **20:** e47182

Brunkard JO, Zambryski PC (2017) Plasmodesmata enable multicellularity: new insights into their evolution, biogenesis, and functions in development and immunity. Curr Opin Plant Biol **35:** 76-83

Eklund DM, Kanei M, Flores-Sandoval E, Ishizaki K, Nishihama R, Kohchi T., et al. (2018) An evolutionarily conserved abscisic acid signaling pathway regulates dormancy in the liverwort *Marchantia polymorpha*. Curr Biol **28:** 3691-3699.e3

Fernandez-Calvino L, Faulkner C, Walshaw J, Saalbach G, Bayer E, Benitez-Alfonso Y., et al. (2011) Arabidopsis plasmodesmal proteome. PLoS One **6:** e18880

Gerlitz N, Gerum R, Sauer N, Stadler R (2018) Photoinducible DRONPA-s: a new tool for investigating cell-cell connectivity. Plant J **94:** 751-766

Golovina EA, Hoekstra FA, Van Aelst AC (2001) The competence to acquire cellular desiccation tolerance is independent of seed morphological development. J Exp Bot

52: 1015-1027

Han X, Kim J-Y (2016) Integrating hormone- and micromolecule-mediated signaling with plasmodesmal communication. Mol Plant **9:** 46-56

Kawade K, Tanimoto H (2015) Mobility of signaling molecules: the key to deciphering plant organogenesis. J Plant Res **128:** 17-25

Kawade K, Tanimoto H, Horiguchi G, Tsukaya H (2017) Spatially different tissue-scale diffusivity shapes ANGUSTIFOLIA3 gradient in growing leaves. Biophys J **113:** 1109-1120

Khandelwal A, Cho SH, Marella H, Sakata Y, Perroud PF, Pan A., et al. (2010) Role of ABA and ABI3 in desiccation tolerance. Science **327:** 546-546

Khraiwesh B, Qudeimat E, Thimma M, Chaiboonchoe A, Jijakli K, Alzahmi A., et al. (2015) Genome-wide expression analysis offers new insights into the origin and evolution of *Physcomitrella patens* stress response. Sci Rep **5:** 17434

Kitagawa M, Fujita T (2013) Quantitative imaging of directional transport through plasmodesmata in moss protonemata via single-cell photoconversion of Dendra2. J Plant Res **126:** 577-585

Kitagawa, M. and Fujita, T. (2015) A model system for analyzing intercellular communication through plasmodesmata using moss protonemata and leaves. J. Plant Res. **128:** 63–72.

Kitagawa M, Tomoi T, Fukushima T, Sakata Y, Sato M, Toyooka K., et al. (2019) Abscisic acid acts as a regulator of molecular trafficking through plasmodesmata in the moss *Physcomitrella patens*. Plant Cell Physiol **60:** 738-751

Komatsu K, Nishikawa Y, Ohtsuka T, Taji T, Quatrano RS, Tanaka S., et al. (2009) Functional analyses of the ABI1-related protein phosphatase type 2C reveal evolutionarily conserved regulation of abscisic acid signaling between Arabidopsis and the moss *Physcomitrella patens*. Plant Mol Biol **70:** 327-340

Komatsu K, Suzuki N, Kuwamura M, Nishikawa Y, Nakatani M, Ohtawa H., et al. (2013) Group A PP2Cs evolved in land plants as key regulators of intrinsic desiccation tolerance. Nat Commun **4:** 2219

Koornneef M, Reuling G, Karssen CM (1984) The isolation and characterization of abscisic acid-insensitive mutants of *Arabidopsis thaliana*. Physiol Plant **61:** 377-383

Kubo M, Imai A, Nishiyama T, Ishikawa M, Sato Y, Kurata T., et al. (2013) System for stable β-estradiol-inducible gene expression in the moss *Physcomitrella patens*. PLoS One **8:** 13

Lee JY (2014) New and old roles of plasmodesmata in immunity and parallels to tunneling nanotubes. Plant Sci **221:** 13-20

Levy A, Zheng JY, Lazarowitzl SG (2015) Synaptotagmin SYTA forms ER-plasma membrane junctions that are recruited to plasmodesmata for plant virus movement. Curr Biol **25:** 2018-2025

Li JX, Wang XQ, Watson MB, Assmann SM (2000) Regulation of abscisic acid-induced stomatal closure and anion channels by guard cell AAPK kinase. Science **287:** 300-303

Ma Y, Szostkiewicz I, Korte A, Moes D, Yang Y, Christmann A., et al. (2009) Regulators of PP2C phosphatase activity function as abscisic acid sensors. Science **324:** 1064-1068

Marella HH, Sakata Y, Quatrano RS (2006) Characterization and functional analysis of *ABSCISIC ACID INSENSITIVE3*-like genes from *Physcomitrella patens*. Plant J **46:** 1032-1044

Minami A, Nagao M, Ikegami K, Koshiba T, Arakawa K, Fujikawa S., et al. (2005) Cold acclimation in bryophytes: low-temperature-induced freezing tolerance in *Physcomitrella patens* is associated with increases in expression levels of stress-related genes but not with increase in level of endogenous abscisic acid. Planta **220:** 414-423

Mustilli AC, Merlot S, Vavasseur A, Fenzi F, Giraudat J (2002) Arabidopsis OST1 protein kinase mediates the regulation of stomatal aperture by abscisic acid and acts upstream of reactive oxygen species production. Plant Cell **14:** 3089-3099

Nagao M, Minami A, Arakawa K, Fujikawa S, Takezawa D (2005) Rapid degradation of starch in chloroplasts and concomitant accumulation of soluble sugars associated with

ABA-induced freezing tolerance in the moss *Physcomitrella patens*. J Plant Physiol **162:** 169-180

Nagao M, Oku K, Minami A, Mizuno K, Sakurai M, Arakawa K., et al. (2006) Accumulation of theanderose in association with development of freezing tolerance in the moss *Physcomitrella patens*. Phytochemistry **67:** 702-709

Nakashima K, Fujita Y, Kanamori N, Katagiri T, Umezawa T, Kidokoro S., et al. (2009) Three Arabidopsis SnRK2 protein kinases, SRK2D/SnRK2.2, SRK2E/SnRK2.6/OST1 and SRK2I/SnRK2.3, involved in ABA signaling are essential for the control of seed development and dormancy. Plant Cell Physiol **50:** 1345-1363

Nishiyama T, Hiwatashi Y, Sakakibara K, Kato M, Hasebe M (2000) Tagged mutagenesis and gene-trap in the moss, *Physcomitrella patens* by shuttle mutagenesis. DNA Res **7:** 9-17

Oldenhof H, Wolkers WF, Bowman JL, Tablin F, Crowe JH (2006) Freezing and desiccation tolerance in the moss *Physcomitrella patens*: An in situ Fourier transform infrared spectroscopic study. Biochim Biophys Acta-Gen Subj **1760:** 1226-1234

Park SY, Fung P, Nishimura N, Jensen DR, Fujii H, Zhao Y., et al. (2009) Abscisic acid inhibits type 2C protein phosphatases via the PYR/PYL family of START proteins. Science **324:** 1068-1071

Perez-Sancho J, Vanneste S, Lee E, McFarlane HE, del Valle AE, Valpuesta V., et al. (2015) The Arabidopsis synaptotagmin1 is enriched in endoplasmic reticulum-plasma membrane contact sites and confers cellular resistance to mechanical stresses. Plant Physiol **168:** 132-143

Rensing SA, Lang D, Zimmer AD, Terry A, Salamov A, Shapiro H., et al. (2008) The *Physcomitrella* genome reveals evolutionary insights into the conquest of land by plants. Science **319:** 64-69

Rowntree JK, Duckett JG, Mortimer CL, Ramsay MM, Pressel S (2007) Formation of specialized propagules resistant to desiccation and cryopreservation in the threatened moss *Ditrichum plumbicola* (Ditrichales, Bryopsida). Ann Bot **100:** 483-496

Saatian B, Austin RS, Tian G, Chen C, Nguyen V, Kohalmi SE., et al. (2018) Analysis of a

novel mutant allele of *GSL8* reveals its key roles in cytokinesis and symplastic trafficking in Arabidopsis. BMC Plant Biol **18:** 295

Sadovsky RG, Brielle S, Kaganovich D, England JL (2017) Measurement of rapid protein diffusion in the cytoplasm by photo-converted intensity profile expansion. Cell Rep **18:** 2795-2806

Saruhashi M, Ghosh TK, Arai K, Ishizaki Y, Hagiwara K, Komatsu K., et al. (2015) Plant Raf-like kinase integrates abscisic acid and hyperosmotic stress signaling upstream of SNF1-related protein kinase2. Proc Natl Acad Sci USA **112:** E6388-E6396

Schapire AL, Voigt B, Jasik J, Rosado A, Lopez-Cobollo R, Menzel D., et al. (2008) *Arabidopsis* synaptotagmin 1 is required for the maintenance of plasma membrane integrity and cell viability. Plant Cell **20:** 3374-3388

Schnepf E, Reinhard C (1997) Brachycytes in *funaria* protonemate: Induction by abscisic acid and fine structure. J Plant Physiol **151:** 166-175

Shinozawa A, Otake R, Takezawa D, Umezawa T, Komatsu K, Tanaka K., et al. (2019) SnRK2 protein kinases represent an ancient system in plants for adaptation to a terrestrial environment. Commun Biol **2:** 30

Stevenson SR, Kamisugi Y, Trinh CH, Schmutz J, Jenkins JW, Grimwood J., et al. (2016) Genetic analysis of *Physcomitrella patens* identifies *ABSCISIC ACID NON-RESPONSIVE*, a regulator of ABA responses unique to basal land plants and required for desiccation tolerance. Plant Cell **28:** 1310-1327

Takezawa D, Watanabe N, Ghosh TK, Saruhashi M, Suzuki A, Ishiyama K., et al. (2015) Epoxycarotenoid-mediated synthesis of abscisic acid in *Physcomitrella patens* implicating conserved mechanisms for acclimation to hyperosmosis in embryophytes. New Phytol **206:** 209-219

Tan TH, Sun YN, Peng XJ, Wu GC, Bao F, He YK., et al. (2017) *ABSCISIC ACID INSENSITIVE3* is involved in cold response and freezing tolerance regulation in *Physcomitrella patens*. Front Plant Sci **8:** 1599

Tylewicz S, Petterle A, Marttila S, Miskolczi P, Azeez A, Singh RK., et al. (2018) Photoperiodic control of seasonal growth is mediated by ABA acting on cell-cell

communication. Science **360:** 212-214

Umezawa T, Sugiyama N, Mizoguchi M, Hayashi S, Myouga F, Yamaguchi-Shinozaki K., et al. (2009) Type 2C protein phosphatases directly regulate abscisic acid-activated protein kinases in *Arabidopsis*. Proc Natl Acad Sci USA **106:** 17588-17593

Umezawa T, Sugiyama N, Takahashi F, Anderson JC, Ishihama Y, Peck SC., et al. (2013) Genetics and phosphoproteomics reveal a protein phosphorylation network in the abscisic acid signaling pathway in *Arabidopsis thaliana*. Sci Signal **6:** 270

Verkman AS (2002) Solute and macromolecule diffusion in cellular aqueous compartments. Trends Biochem Sci **27:** 27-33

Vlad F, Rubio S, Rodrigues A, Sirichandra C, Belin C, Robert N., et al. (2009) Protein phosphatases 2C regulate the activation of the Snf1-related kinase OST1 by abscisic Acid in *Arabidopsis*. Plant Cell **21:** 3170-3184

Wang PC, Xue L, Batelli G, Lee S, Hou YJ, Van Oosten MJ., et al. (2013) Quantitative phosphoproteomics identifies SnRK2 protein kinase substrates and reveals the effectors of abscisic acid action. Proc Natl Acad Sci USA **110:** 11205-11210

Wolkers WF, Alberda M, Koornneef M, Leon-Kloosterziel KM, Hoekstra FA (1998) Properties of proteins and the glassy matrix in maturation-defective mutant seeds of *Arabidopsis thaliana*. Plant J **16:** 133-143

Wu S, Koizumi K, MacRae-Crerar A, Gallagher KL (2011) Assessing the utility of photoswitchable fluorescent proteins for tracking intercellular protein movement in the *Arabidopsis* root. PLoS One **6:** e27536

Wu SW, Kumar R, Iswanto ABB, Kim JY (2018) Callose balancing at plasmodesmata. J Exp Bot **69:** 5325-5339

Yoshida R, Hobo T, Ichimura K, Mizoguchi T, Takahashi F, Aronso J., et al. (2002) ABA-activated SnRK2 protein kinase is required for dehydration stress signaling in *Arabidopsis*. Plant Cell Physiol **43:** 1473-1483

Yoshida T, Christmann A, Yamaguchi-Shinozaki K, Grill E, Fernie AR (2019) Revisiting the basal role of ABA - roles outside of stress. Trends Plant Sci **24:** 625-635

Yotsui I, Serada S, Naka T, Saruhashi M, Taji T, Hayashi T., et al. (2016) Large-scale

proteome analysis of abscisic acid and ABSCISIC ACID INSENSITIVE3-dependent proteins related to desiccation tolerance in *Physcomitrella patens*. Biochem Biophys Res Commun **471:** 589-595

Zavaliev R, Epel BL (2015) Imaging callose at plasmodesmata using aniline blue: quantitative confocal microscopy. Methods Mol Biol 1217, 105-119

Zhao MK, Li QL, Chen ZH, Lv Q, Bao F, Wang XQ., et al. (2018) Regulatory mechanism of ABA and ABI3 on vegetative development in the moss *Physcomitrella patens*. Int J Mol Sci **19:** 2728

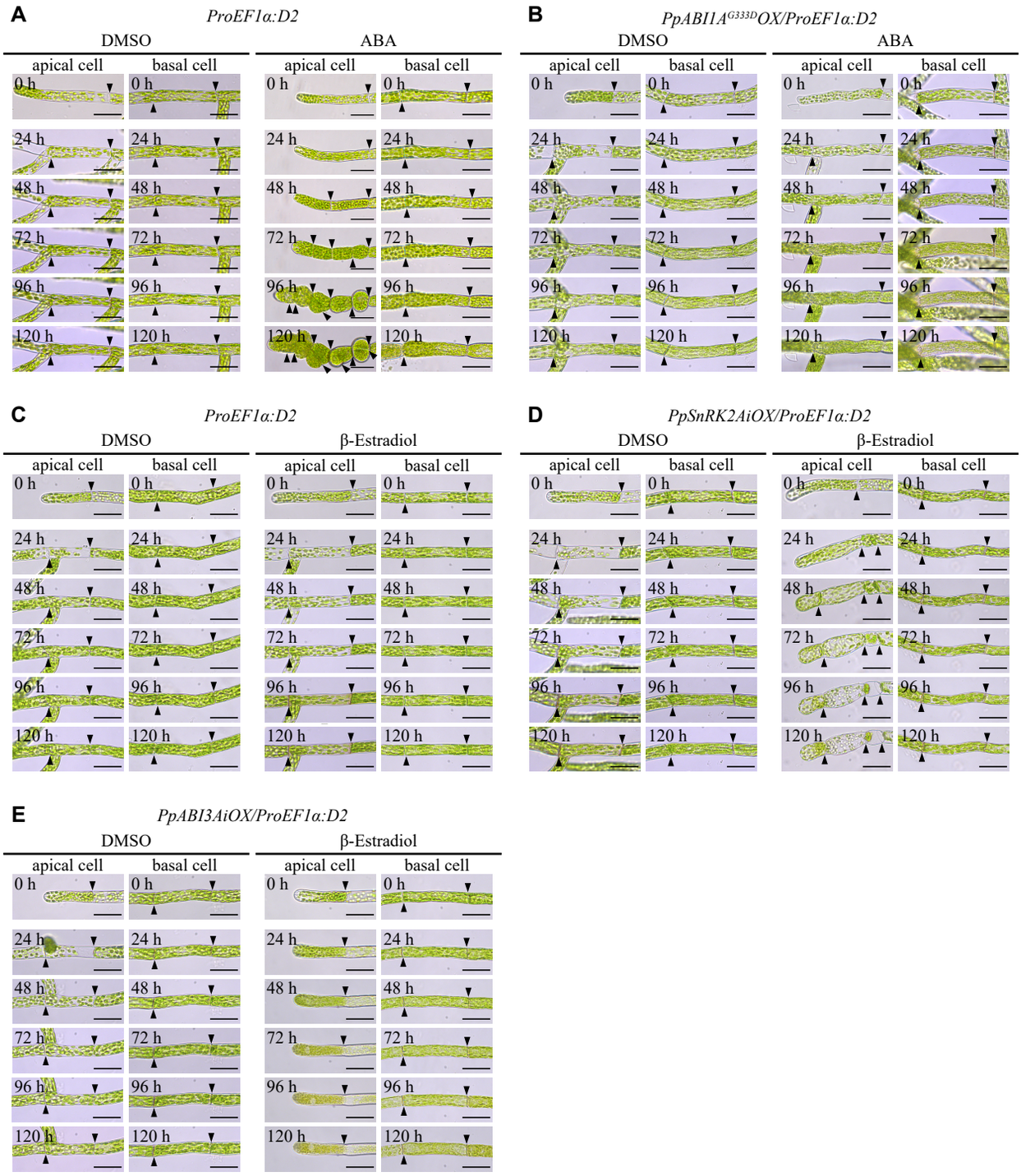

Figure 1. Morphology and growth of protonemal cells in transgenic lines overexpressing *PpABI1A*^{G333D}, *PpSnRK2A*, or *PpABI3A*.

A and B, Representative images of protonemal cells at apical and basal positions after DMSO or ABA treatment in *ProEF1α:D2* (A) and *PpABI1A*^{G333D}*OX/ProEF1α:D2* (B). C to E, Representative images of protonemal cells at apical and basal positions after DMSO or β-estradiol treatment in *ProEF1α:D2* (C), *PpSnRK2AiOX/ProEF1α:D2* (D), and *PpABI3AiOX/ProEF1α:D2* (E). Times after treatment are indicated. The 12th cells were observed as the basal cells. Scale bars = 50 μm. Arrowheads indicate cross walls of the original branches.

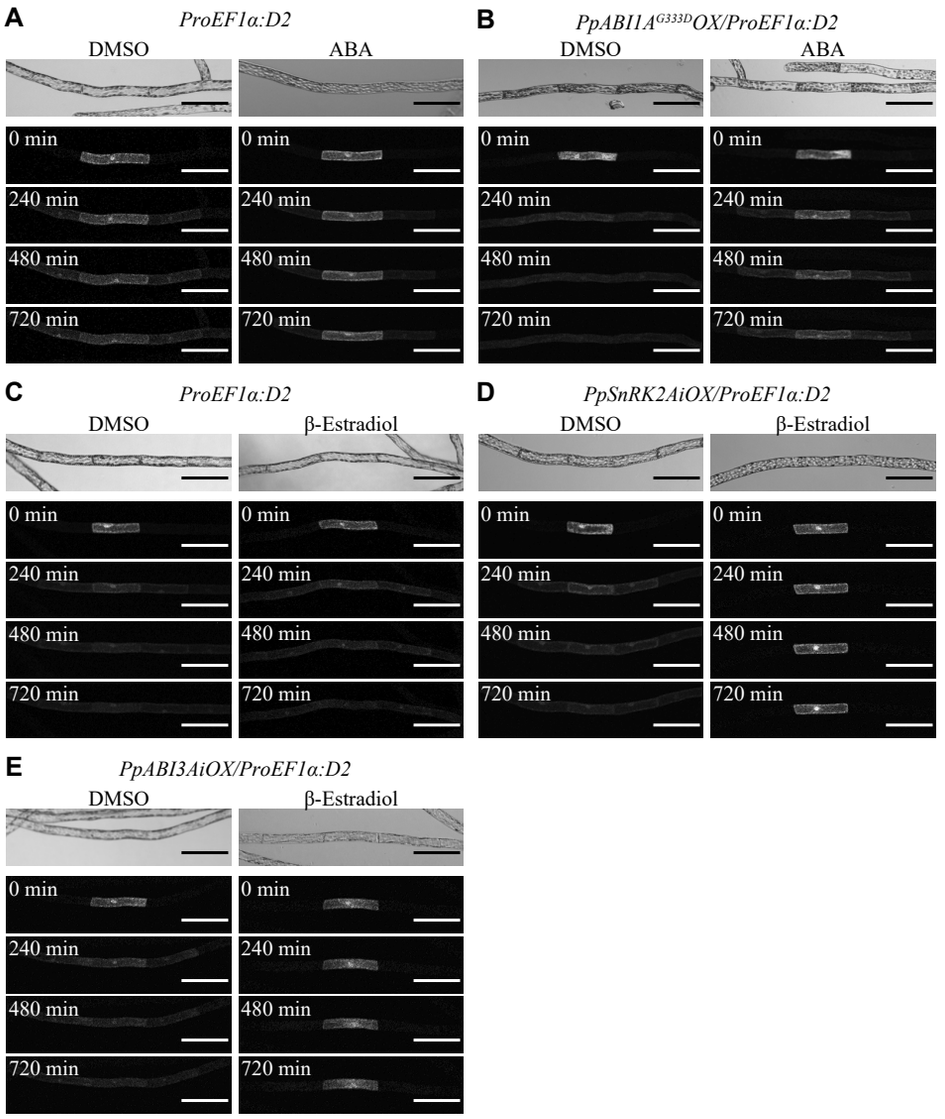

Figure 2. Dendra2 movement between protonemal cells in transgenic lines overexpressing *PpABI1A*^{G333D}, *PpSnRK2A*, or *PpABI3A*.

A and B, Representative differential interference contrast (DIC) and photoconverted Dendra2 fluorescence (gray) images in protonemal cells of *ProEF1α:D2* (A) and *PpABI1A*^{G333D}*OX/ProEF1α:D2* (B) treated with DMSO or ABA. C to E, Representative DIC and photoconverted Dendra2 fluorescence (gray) images in protonemal cells of *ProEF1α:D2* (C), *PpSnRK2AiOX/ProEF1α:D2* (D), and *PpABI3AiOX/ProEF1α:D2* (E) treated with DMSO or β-estradiol. Times after photoconversion are indicated. Scale bars = 100 μm.

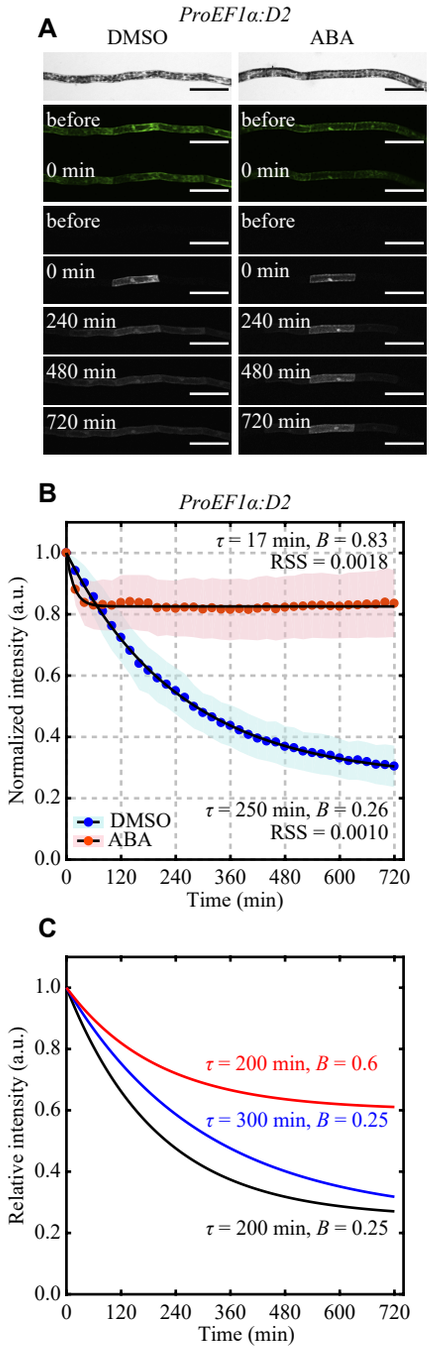
A
ProEF1α:D2
DMSO
ABA
before
0 min
240 min
480 min
720 min
B
ProEF1α:D2
τ = 17 min, B = 0.83
RSS = 0.0018
τ = 250 min, B = 0.26
RSS = 0.0010
DMSO
ABA
Normalized intensity (a.u.)
Time (min)
C
τ = 200 min, B = 0.6
τ = 300 min, B = 0.25
τ = 200 min, B = 0.25
Relative intensity (a.u.)
Time (min)

Figure 3. Quantitative characterization of Dendra2 movement between protonemal cells and its suppression by ABA.

A, Representative DIC, non-photoconverted (green), and photoconverted (gray) Dendra2 fluorescence images in protonemal cells of *ProEF1α:D2* treated with DMSO or ABA. Times after photoconversion are indicated. Scale bars = 100 μm. B, Mean fluorescence intensity of Dendra2 at 20-min intervals after photoconversion in photoconverted protonemal cells of *ProEF1α:D2* treated with DMSO (n = 15) or ABA (n = 27). Standard deviation (SD) is indicated by shaded area. The time constant (τ) and immobile fraction (B) were determined by fitting the exponential function to the kinetics of mean fluorescence intensity (black solid lines). RSS, residual sum of squares. C, Schematic diagram of kinetics obtained by using different combinations of fitting parameters. Intercellular diffusivity of macromolecules is determined by τ and B. Highly permeable PD allow Dendra2 to move more rapidly from the original cell (black) than lower permeable PD (blue). More Dendra2 is trapped in the original cell when immobile fraction is increased (red).

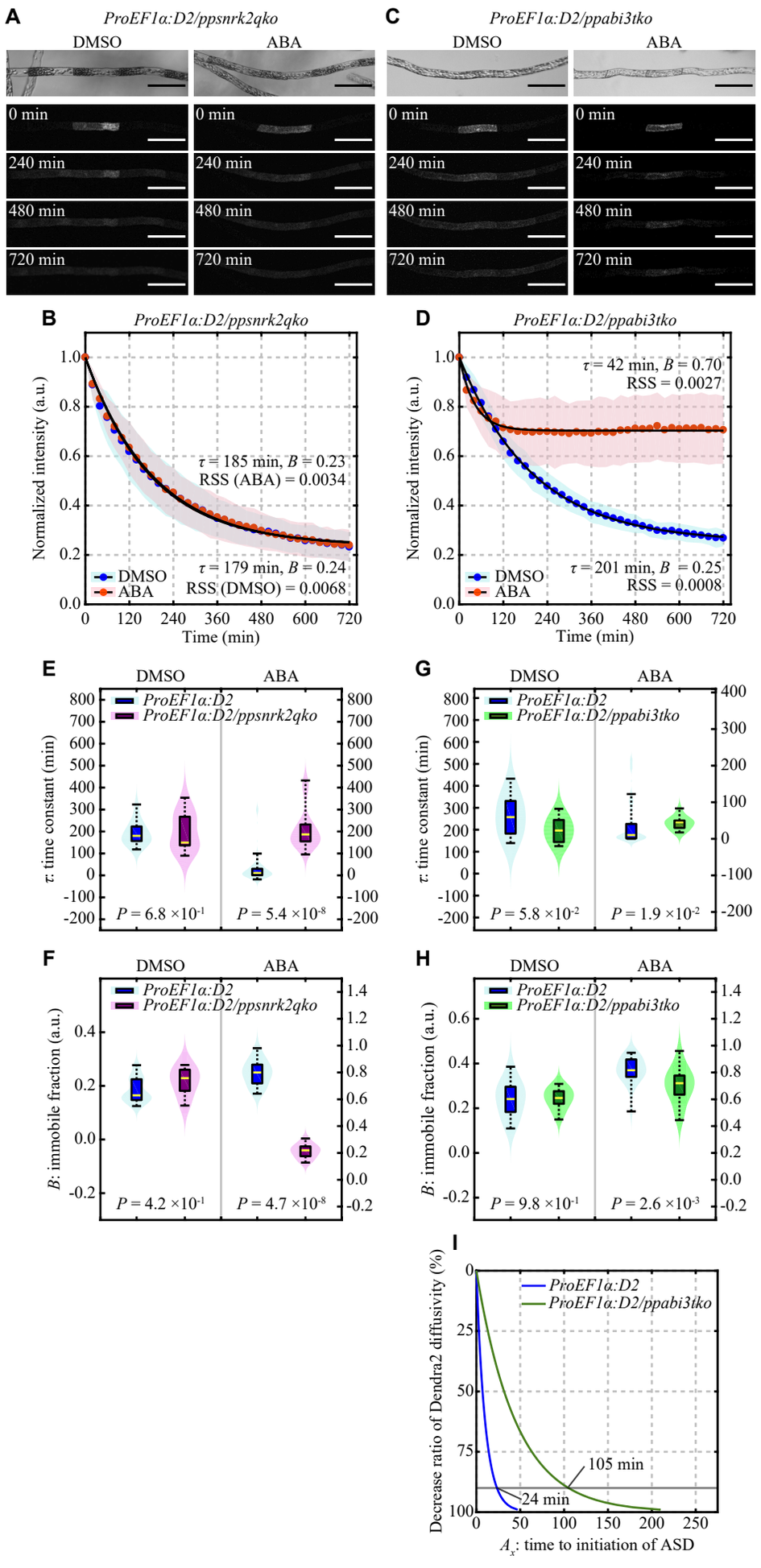
A
ProEF1α:D2/ppsnrk2qko
DMSO
ABA
0 min
240 min
480 min
720 min
C
ProEF1α:D2/ppabi3tko
B
ProEF1α:D2/ppsnrk2qko
Normalized intensity (a.u.)
τ = 185 min, B = 0.23
RSS (ABA) = 0.0034
τ = 179 min, B = 0.24
RSS (DMSO) = 0.0068
Time (min)
D
ProEF1α:D2/ppabi3tko
τ = 42 min, B = 0.70
RSS = 0.0027
τ = 201 min, B = 0.25
RSS = 0.0008
E
τ: time constant (min)
ProEF1α:D2
ProEF1α:D2/ppsnrk2qko
P = 6.8 ×10-1
P = 5.4 ×10-8
G
ProEF1α:D2/ppabi3tko
P = 5.8 ×10-2
P = 1.9 ×10-2
F
B: immobile fraction (a.u.)
P = 4.2 ×10-1
P = 4.7 ×10-8
H
P = 9.8 ×10-1
P = 2.6 ×10-3
I
Decrease ratio of Dendra2 diffusivity (%)
105 min
24 min
Ax: time to initiation of ASD

Figure 4. Intercellular Dendra2 diffusivity in protonemal cells of *ProEF1α:D2/ppsnrk2qko* and *ProEF1α:D2/ppabi3tko.*

A and C, Representative DIC and photoconverted Dendra2 fluorescence (gray) images in protonemal cells of *ProEF1α:D2/ppsnrk2qko* (A) and *ProEF1α:D2/ppabi3tko* (C) treated with DMSO or ABA. Times after photoconversion are indicated. Scale bars = 100 μm. B and D, Mean fluorescence intensity of Dendra2 at 20-min intervals after photoconversion in protonemal cells of *ProEF1α:D2/ppsnrk2qko* (B) and *ProEF1α:D2/ppabi3tko* (D) treated with DMSO or ABA with exponential fits to the mean data. SD is indicated by the shaded area. The τ and *B* were determined by fitting the exponential function to the kinetics of mean fluorescence intensity (black solid lines). E to H, Values of the time constant τ and *B* obtained through the fittings. The τ and *B* in *ProEF1α:D2* and *ProEF1α:D2/ppsnrk2qko* (E and F), and in *ProEF1α:D2* and *ProEF1α:D2/ppabi3tko* (G and H). Each violin plot shows the density distribution of the data by the box plot (median as a yellow horizontal line, interquartile range as a box, and data range as whiskers). The *P* value was determined by the Mann-Whitney *U*-test. *ProEF1α:D2* with DMSO (n = 17) and ABA (n = 24) (E and F), and *ProEF1α:D2/ppsnrk2qko* with DMSO (n = 13) and ABA (n = 22) (B, E and F). *ProEF1α:D2* with DMSO (n = 15) and ABA (n = 27) (G and H), and *ProEF1α:D2/ppabi3tko* with DMSO (n = 14) and ABA (n = 17) (D, G and H). I, Time to initiation of ASD calculated from the median of fitting parameters in *ProEF1α:D2* and *ProEF1α:D2/ppabi3tko*. The grey line indicates A_{90}.

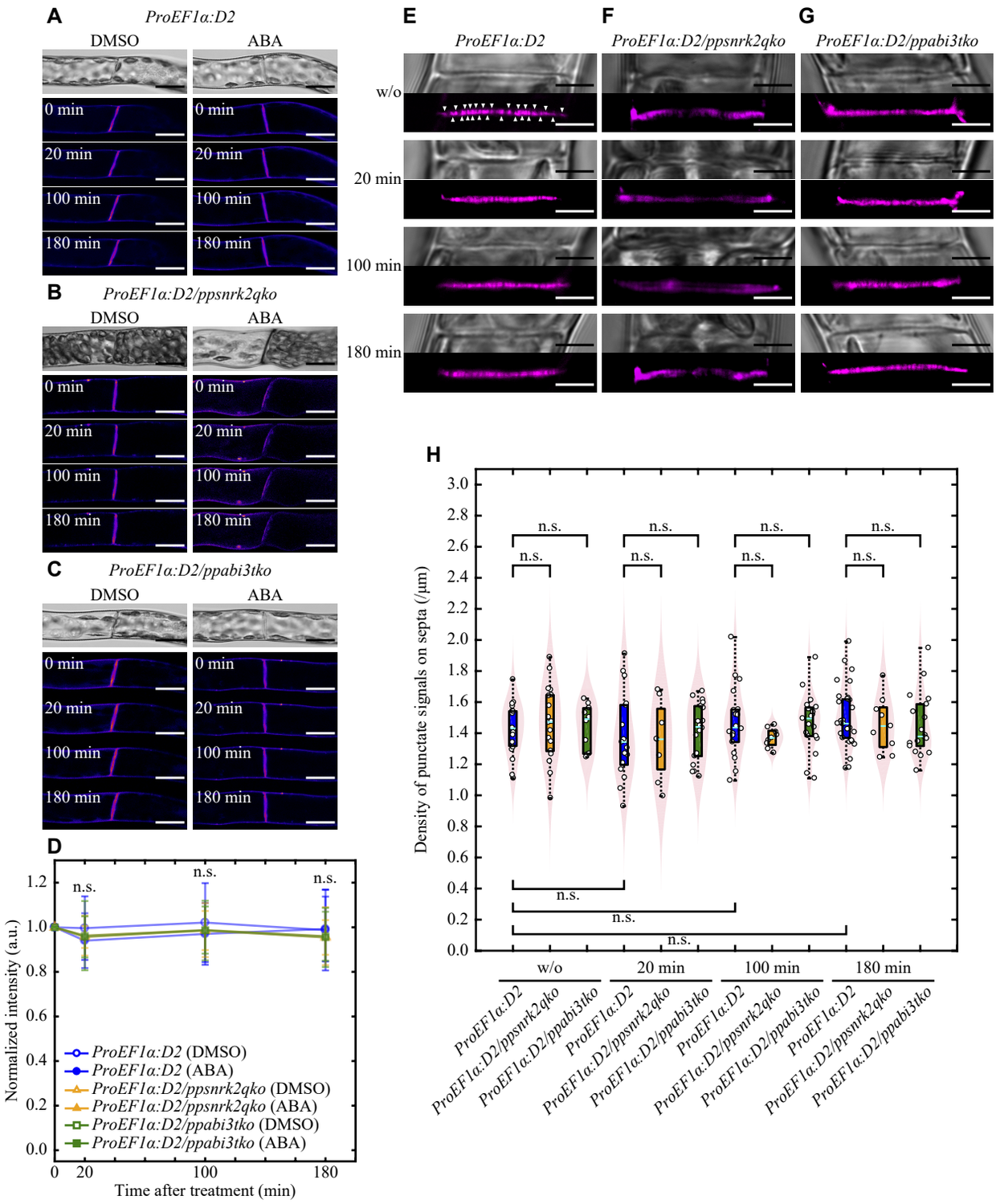
A
ProEF1α:D2
DMSO
ABA
0 min
20 min
100 min
180 min
B
ProEF1α:D2/ppsnrk2qko
C
ProEF1α:D2/ppabi3tko
D
n.s.
Normalized intensity (a.u.)
ProEF1α:D2 (DMSO)
ProEF1α:D2 (ABA)
ProEF1α:D2/ppsnrk2qko (DMSO)
ProEF1α:D2/ppsnrk2qko (ABA)
ProEF1α:D2/ppabi3tko (DMSO)
ProEF1α:D2/ppabi3tko (ABA)
Time after treatment (min)
E
F
G
ProEF1α:D2/ppsnrk2qko
ProEF1α:D2/ppabi3tko
w/o
20 min
100 min
180 min
H
Density of punctate signals on septa (/μm)
n.s.
w/o
20 min
100 min
180 min
ProEF1α:D2
ProEF1α:D2/ppsnrk2qko
ProEF1α:D2/ppabi3tko

Figure 5. Live-cell imaging of aniline blue staining for callose after ABA treatment.

A ~~and~~to ~~B~~C, Representative images of DIC and aniline blue fluorescence for callose staining in protonemal cells of *ProEF1α:D2* (A), *ProEF1α:D2/ppsnrk2qko* (B), and *ProEF1α:D2/ppabi3tko* (~~B~~C) after DMSO or ABA treatment. Times after treatment are indicated. The callose signal is shown in Fire look-up table of ImageJ. Scale bars = 20 μm. ~~C~~D, Change in aniline blue fluorescence intensity on cross walls in protonemal cells of *ProEF1α:D2*, *ProEF1α:D2/ppsnrk2qko*, and *ProEF1α:D2/ppabi3tko* after DMSO or ABA treatment. *ProEF1α:D2* with DMSO (n = 12) and ABA (n = 12), *ProEF1α:D2/ppsnrk2qko* with DMSO (n = 12) and ABA (n = 8), and *ProEF1α:D2/ppabi3tko* with DMSO (n = 10) and ABA (n = 12). The P value was determined by the Welch's t-test, n.s., non-significance (P ~~>~~≥ 0.05). ~~D and E~~E to G, Representative images of DIC and punctate callose signal of aniline blue fluorescence at cross walls between the 11th and 12th cell of *ProEF1α:D2* (~~D~~E), *ProEF1α:D2/ppsnrk2qko* (F), and *ProEF1α:D2/ppabi3tko* (G) protonemal cells ~~(E)~~ after ABA treatment. Times after treatment are indicated. Scale bars = 5 μm. Arrowheads indicate punctate signals included in the number as an example (~~D~~E). ~~F~~H, The ~~number~~density of punctate signals on cross walls between the 11th and 12th cell in *ProEF1α:D2*, *ProEF1α:D2/ppsnrk2qko*, and *ProEF1α:D2/ppabi3tko* after ABA treatment. Each violin plot shows the density distribution of the data by the box plot (median as a ~~yellow~~cyan horizontal line, interquartile range as a box, and data range as whiskers). *ProEF1α:D2* without and after 20-, 100- and 180-min ABA treatment (n = 19, 17, 18 and 30, respectively), *ProEF1α:D2/ppsnrk2qko* without and after 20-, 100- and 180-min ABA treatment (n = 18, 8, 9 and 9, respectively), and *ProEF1α:D2/ppabi3tko* without and after 20-, 100- and 180-min ABA treatment (n = 10, 18, 19 and 18, respectively). The P value was determined by the Mann-Whitney U-test, n.s., non-significance P ~~>~~≥ 0.05).

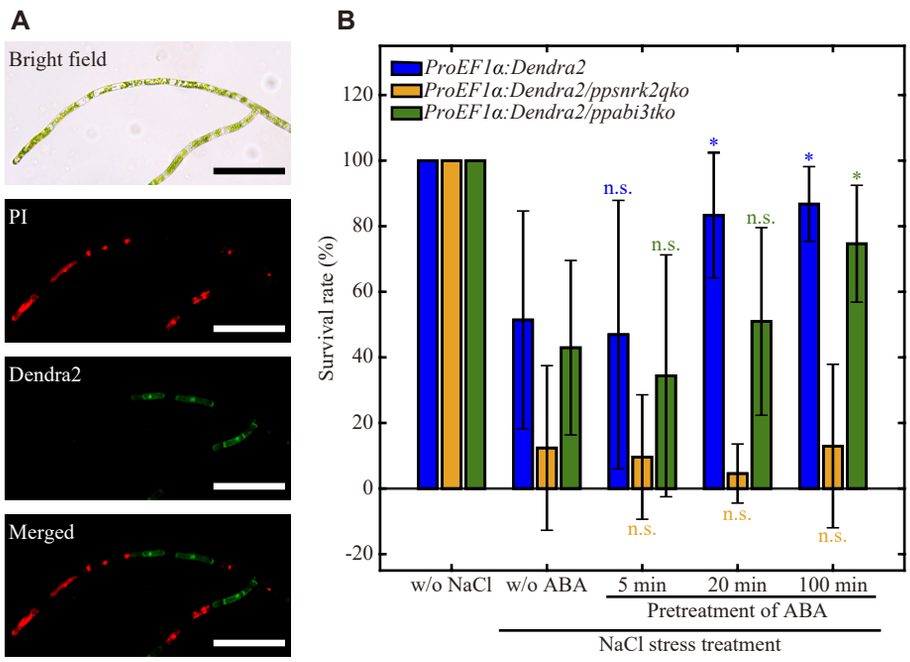

Figure 6. Viability under salt stress after different pretreatment time of ABA.

A, Representative bright field, PI and non-photoconverted Dendra2 fluorescence images after the salt stress treatment. Cells with PI signal indicate dead cells. B, Survival rate after the salt stress with ABA pretreatment. "w/o NaCl" indicates the condition without salt stress and ABA treatment. The bar graph shows mean ± SD of the survival rate (n = 75). The P value was determined by the Mann-Whitney U-test, n.s., non-significance ($P \geq 0.05$), *$P < 0.01$ compared to the non-ABA pretreated corresponding line.